This article has been accepted for publication in IEEE Sensors Journal. This is the author's version which has not been fully edited and content may change prior to final publication. Citation information: DOI 10.1109/JSEN.2026.3668988

Precision Sensing at Selected Spectrum: A Double-Negative Low-Cost Metamaterial Sensor with Enhanced Directionality for Biomedical Applications

Musa N. Hamza, Mohammad Tariqul Islam, Slawomir Koziel, Sunil Lavadiya, Iftikhar ud Din, Bruno Sanches, Syeda Iffat Naqvi, Abinash Panda, Mohammad Naser-Moghadasi, Bal Virdee, Ali Farmani, Patrizia Livreri, Md. Shabiul Islam, Nisar Ahmad Abbasi, and Mohammad Alibakhshikenari

***Abstract*— This paper presents a novel, low-cost, compact sensor that integrates a double-negative (DNG) metamaterial with an artificial magnetic conductor (AMC)-backed microstrip patch antenna, specifically optimized for high-precision biomedical applications in the 2–4 GHz range. Unlike prior designs, the proposed sensor leverages the simultaneous negative permittivity and permeability of the DNG structure together with the AMC layer to achieve enhanced gain, directionality, and sensitivity—key performance factors for GHz-range diagnostics. Fabricated on a cost-effective FR4 substrate with a compact footprint of 50 × 50 mm², the sensor is well-suited for scalable, real-world deployment. Full-wave simulations confirm negative refractive index characteristics within the 2.0–2.7 GHz band, and a peak gain of 7.6 dBi is achieved, surpassing comparable designs. Experimental validation in an anechoic chamber shows excellent agreement with simulation results. Benchmarking demonstrates that the sensor outperforms state-of-the-art counterparts in gain, size, and directional response. These features make it a strong candidate for biomedical applications such as wearable health monitoring, portable medical imaging, and non-invasive diagnostics including early-stage brain abnormality detection.**

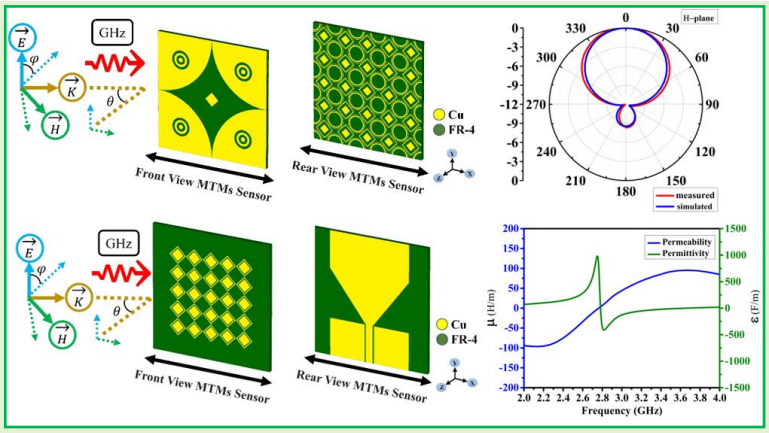

***Index Terms*— Double-Negative Metamaterials; Biomedical Sensor; AMC Integration; High-Gain Compact Sensors; Electromagnetic Wave Manipulation**

I. Introduction

Metamaterials represent one of the most transformative frontiers in modern science and engineering, offering unique electromagnetic behaviors not found in naturally occurring materials. These artificially engineered structures derive their properties not from their chemical composition but from their subwavelength-scale architecture, enabling unprecedented control over wave propagation phenomena such as reflection, refraction, and absorption [1, 2]. Among their most striking characteristics is the ability to exhibit a negative refractive index, allowing electromagnetic waves to bend in the opposite direction compared to conventional materials. This capability has led to a wide range of innovations across disciplines.

Co-funded by the European Union. Views and opinions expressed are however those of the author(s) only and do not necessarily reflect those of the European Union or the European Research Executive Agency. Neither the European Union nor the granting authority can be held responsible for them. Besides that, this publication has emanated from research jointly funded by Taighde Éireann – Research Ireland under Grant number 13/RC/2094_2, the European Union's Marie Sklodowska-Curie Actions under grant number 101126578 and was supported in part by University of Galway. The authors gratefully acknowledge the financial support of the University of Doha for Science and Technology under Grant No. KK-2024-005. Additionally, part of this research has been supported by the Icelandic Research Fund (Grant No. 2410297) and the National Science Centre of Poland (Grant No. 2022/47/B/ST7/00072). (Corresponding authors: Musa N. Hamza; Mohammad Tariqul Islam; Md. Shabiul Islam; Mohammad Alibakhshikenari)

Musa N. Hamza is with Department of Physics, College of Science, University of Raparin, Sulaymaniyah 46012, Iraq. (e-mail: musa.nuraden@uor.edu.krd).

Mohammad Tariqul Islam is with Department of Electrical, Electronic and Systems Engineering, Faculty of Engineering and Built Environment, Universiti Kebangsaan Malaysia, 43600 UKM Bangi, Selangor, Malaysia. (e-mail: tariqul@ukm.edu.my).

Mohammad Tariqul Islam is with Computer and Information Sciences Research Center (CISRC), Imam Mohammad Ibn Saud Islamic University (IMSIU), Riyadh, Saudia Arabia.

Slawomir Koziel is with Engineering Optimization & Modeling Center, Reykjavik University, 102 Reykjavik, Iceland.

Slawomir Koziel is also with Faculty of Electronics, Telecommunications and Informatics, Gdansk University of Technology, 80-233 Gdansk, Poland. (e-mail: Koziel@ru.is).

Sunil Lavadiya is with Department of Information and Communication Technology, Marwadi University, Rajkot-360003, Gujarat, India. (e-mail: sunil.lavadiya@marwadieducation.edu.in).

Iftikhar ud Din is with Telecommunication Engineering Department, University of Engineering and Technology, Mardan 23200, Pakistan. (e-mail: iftikharuddin114@gmail.com).

Bruno Sanches is with Department of Electronic Systems Engineering, Escola Politécnica da Universidade de São Paulo São Paulo, Brazil. (e-mail: bruno.csanches@usp.br).

Syeda Iffat Naqvi is with Department of Telecommunication Engineering University of Engineering & Technology Taxila, Pakistan. (e-mail: iffat.naqvi@uettaxila.edu.pk).

Abinash Panda is with Department of Electronics and Communication Engineering, CMR Institute of Technology, Bengaluru 560037, India. (e-mail: abinashpanda087@gmail.com).

Mohammad Naser-Moghadasi is with Computer and Electrical Engineering Department, Science and Research Branch, Islamic Azad University, Tehran 14696-69191, Iran; (e-mail: mo.naser@iau.ac.ir).

Bal Virdee is with Department of Center for Communications Technology, London Metropolitan University, London N7 8DB, United Kingdom; (e-mail:b.virdee@londonmet.ac.uk).

Ali Farmani is with Department of electronics engineering, Lorestan University, Iran. (e-mail: farmani.a@lu.ac.ir).

P. Livreri is with the Department of Engineering, University of Palermo, IT 90128 Palermo, Italy; (e-mail: patrizia.livreri@unipa.it).

Md. Shabiul Islam is with Centre for Advanced Devices and Systems, Centre of Excellence for Robotics and Sensing Technologies, Multimedia University, Persiaran Multimedia, 63100 Cyberjaya, Selangor, Malaysia. (e-mail: shabiul.islam@mmu.edu.my).

Md. Shabiul Islam is with Faculty of Artificial Intelligence and Engineering, Multimedia University, Persiaran Multimedia, 63100 Cyberjaya, Selangor, Malaysia.

N. A. Abbasi is with the Department of Electrical Engineering, School of Systems Engineering, Bahrain Polytechnic, Isa Town, Bahrain; (e-mail: nisar.abbasi@polytechnic.bh).

Mohammad Alibakhshikenari is with the Lero, the Research Ireland Centre for Software, College of Science and Engineering, School of Computer Science, University of Galway, H91 TK33 Galway, Ireland. He is also with the Department of Electrical and Electronics Engineering, Dogus University, 34775 Umraniye, Istanbul, Türkiye; (e-mail: mohammad.alibakhshikenari@universityofgalway.ie).

XXXX-XXXX © XXXX IEEE. Personal use is permitted, but republication/redistribution requires IEEE permission.
See http://www.ieee.org/publications_standards/publications/rights/index.html for more information.
This work is licensed under a Creative Commons Attribution 4.0 License. For more information, see https://creativecommons.org/licenses/by/4.0/

This article has been accepted for publication in IEEE Sensors Journal. This is the author's version which has not been fully edited and
content may change prior to final publication. Citation information: DOI 10.1109/JSEN.2026.3668988

Applications of metamaterials span diverse sectors, including GPS enhancement [3], MIMO antenna isolation improvement [4], radar cross-section reduction [5], military stealth technologies [6], underwater acoustic absorption [7], secure communication via cryptography [8], wavelength-selective thermal detection [9], and high-resolution imaging and explosive detection [10, 11] [12]. Particularly in healthcare applications, metamaterial-based electromagnetic structures have enabled significant advancements in medical imaging, biosensing, and non-invasive diagnostics within the microwave and gigahertz (GHz) frequency ranges. Their engineered permittivity and permeability properties facilitate enhanced field confinement, improved dielectric contrast detection, and compact sensor configurations suitable for wearable and portable biomedical systems. These capabilities have positioned metamaterials as promising platforms for high-precision, label-free diagnostic technologies operating in clinically relevant microwave bands [13-15].

One of the most compelling advantages of metamaterials in sensing lies in their ability to localize and amplify electromagnetic fields. This property enhances the selectivity and sensitivity of sensors, allowing detection of minute changes in material properties or small quantities of target analytes [16-18]. Unlike traditional sensors, metamaterial-based sensors can be tuned to resonate at specific frequencies—microwave, THz, or infrared—making them especially suitable for biomolecular interaction detection. Recent studies have demonstrated their efficacy in identifying proteins, enzymes, pathogens, and environmental contaminants, positioning them as powerful tools in biomedical diagnostics and environmental biosensing [19, 20]. A particularly powerful class of metamaterials is those exhibiting double-negative (DNG) properties, with simultaneous negative permittivity ($\varepsilon < 0$) and permeability ($\mu < 0$). First conceptualized by Veselago in 1968 [21], DNG metamaterials enable phenomena like negative refraction and reverse Doppler effects, making them valuable in applications such as absorbers, antennas, filters, waveguides, polarization converters, lenses, and sensors [22-29]. These properties arise from periodic unit cell structures, such as split-ring resonators (SRRs) for negative permeability and wire arrays for negative permittivity, carefully engineered to resonate at specific frequencies.

DNG-based biosensors capitalize on the extreme wave manipulation capabilities of these metamaterials. When biomolecules bind to a functionalized metamaterial surface, they induce local permittivity changes, resulting in detectable shifts in the resonance frequency. This mechanism enables high-sensitivity detection of biological targets. Moreover, when integrated with microfluidic systems, DNG metamaterial sensors can analyze small-volume samples in real time, making them ideal for point-of-care diagnostics [30].

In parallel, antennas, traditionally used in telecommunications and radar, have emerged as essential components in biosensing. Their ability to interact with electromagnetic fields allows them to detect, convert, and transmit biological signals. Antennas operate as transducers, where molecular binding events or dielectric changes in the surrounding environment are manifested as shifts in resonance frequency, amplitude, or phase [31] [32, 33]. Their non-intrusive, label-free nature makes them highly suitable for applications in healthcare diagnostics, environmental monitoring, and food safety.

Among various antenna types, microstrip patch antennas have become leading candidates for biomedical sensing due to their compact geometry, low profile, straightforward fabrication, and compatibility with planar and wearable platforms [34, 35] [36-40]. However, conventional patch antennas inherently suffer from narrow bandwidth and limited directionality, restricting their sensing resolution and effective range. To address these shortcomings, metamaterial-assisted antenna architectures have been explored, providing enhanced sensitivity, miniaturization, and superior electromagnetic performance across microwave and terahertz frequencies [15, 26, 41-44]. These developments have enabled multifunctional electromagnetic sensors capable of label-free, non-invasive, and high-precision biomedical diagnostics.

Despite this progress, recent advances in microwave metamaterial-based biosensing reveal a persistent need for highly directive, miniaturized, and cost-effective sensor architectures tailored for biomedical environments. Existing studies illustrate the limitations clearly: Patel et al. (2025) proposed a metamaterial-based glucose sensor focused on non-invasive measurement [45]; Douhi et al. (2025) presented an AMC-integrated wearable antenna improving tissue coupling [46]; and Qiang et al. (2025) introduced a symmetric metamaterial element for microfluidic cell detection [47]. Other works, such as those by Maged et al. (2025) [48] and Hossain and Hannan (2025) [49], address wearability and S-band sensing but lack DNG behavior, directional control, or AMC integration. Collectively, these studies underscore the absence of a unified platform combining DNG metamaterial behavior, AMC enhancement, and biomedical-grade sensing in a compact, low-cost design.

Although several recent investigations have explored metamaterial-enhanced microwave sensors or AMC-backed antennas, none have simultaneously demonstrated experimentally validated DNG behavior, high realized gain on FR4, and integrated electromagnetic lensing within a manufacturable footprint suitable for clinical or wearable use. Prior works on DNG resonators [30] [50], metamaterial-assisted biomedical systems [51], and AMC-enhanced wearable antennas [52] consistently highlight trade-offs between sensitivity, directivity, gain, and substrate cost. This establishes a clear technological gap: the lack of a compact, experimentally validated GHz-range biosensor that merges DNG metamaterial lensing with AMC-backed antenna engineering on an FR4 platform. The present work addresses this gap by realizing a dual-functional AMC+DNG sensor with verified performance metrics (gain: 7.6 dBi, sensitivity: 0.4527 GHz·RIU^{-1}, Q-factor: 175.18), offering a practical and scalable route toward next-generation high-precision biomedical sensing.

This study presents a novel GHz-range sensor that uniquely integrates a double-negative metamaterial with an artificial magnetic conductor (AMC)-backed microstrip patch antenna in a compact 50 × 50 mm² configuration. While AMCs and metamaterials have been separately employed in antenna and sensing designs, the originality of this work lies in combining these technologies on a cost-effective FR4 substrate

XXXX-XXXX © XXXX IEEE. Personal use is permitted, but republication/redistribution requires IEEE permission.
See http://www.ieee.org/publications_standards/publications/rights/index.html for more information.
This work is licensed under a Creative Commons Attribution 4.0 License. For more information, see https://creativecommons.org/licenses/by/4.0/

This article has been accepted for publication in IEEE Sensors Journal. This is the author's version which has not been fully edited and
content may change prior to final publication. Citation information: DOI 10.1109/JSEN.2026.3668988

specifically optimized for biomedical use. The sensor is engineered to operate in the 2–4 GHz band and demonstrates high gain (7.6 dBi), sharp directionality, and strong dielectric sensitivity attributes essential for applications such as brain abnormality detection, wearable diagnostics, and portable health monitoring. To the best of our knowledge, this is the first demonstration of a low-cost, compact, AMC-backed DNG metamaterial sensor with validated performance metrics and real-world applicability in GHz-band biomedical scenarios. Both simulation and experimental results confirm the sensor's reliability and competitive advantage over existing designs.

II. Narrowband Sensing with Metamaterial-Based Perfect Lens and AMC

Narrowband sensing technologies that utilize metamaterial-based perfect lenses and AMCs offer innovative routes for enhancing sensor performance in precision applications. These approaches exploit the unique electromagnetic behavior of metamaterials to localize and amplify fields, thereby increasing the sensitivity and resolution of sensors. In particular, double-negative metamaterials (DNGs), which exhibit simultaneous negative permittivity and permeability, are capable of amplifying evanescent waves and enabling perfect lensing, a phenomenon where sub-wavelength details can be resolved beyond the classical diffraction limit.

Metamaterials are highly customizable, and their unit-cell structures can be tailored to produce desired electromagnetic responses at specific frequencies. This tunability makes them especially attractive for narrowband sensor applications where selectivity and high resolution are crucial. When integrated with AMCs, the performance of metamaterial sensors can be further improved. AMCs reflect incident electromagnetic waves with zero phase shift, thereby enhancing antenna and sensor performance by controlling surface currents and suppressing back radiation. This leads to the development of low-profile, high-directivity sensors with compact geometries suitable for integration in biomedical or industrial environments.

Despite these advantages, practical implementation of such sensors remains challenging particularly in achieving precise fabrication, minimizing losses, and tuning the device to resonate within narrow frequency bands.

A. Structural Design and Sensor Configuration

The structural configuration of the proposed metamaterial-based biomedical sensor has been carefully engineered to achieve optimal electromagnetic performance within the 2–4 GHz frequency range. As illustrated in Fig. 1, the architecture integrates a double-negative (DNG) metamaterial with an artificial magnetic conductor (AMC)-backed microstrip patch antenna. This hybrid design enhances field confinement, forward radiation, and dielectric sensitivity, ensuring efficient coupling between the metamaterial unit cells and the incident electromagnetic fields. The resulting localized resonances are essential for accurate and high-resolution biomedical sensing.

To explain the magnetic response of the DNG structure, an analogy is drawn, purely conceptually, to the operating behavior of Magnetic Tunnel Junctions (MTJs). No MTJ devices are used or fabricated in this sensor. Instead, the analogy helps illustrate how adjacent resonant elements within the DNG array support controlled magnetic interactions. These interactions, driven by alternating surface currents and coupled magnetic resonances, behave similarly to the tunable magnetoresistive effects seen in MTJ structures. This conceptual comparison provides intuitive insight into how the DNG–AMC combination achieves stable magnetic-field behavior and enhanced sensitivity.

By using this analogy as a descriptive model, the magnetic resonance dynamics and field-coupling behavior in the hybrid DNG–AMC system can be better understood. It clarifies how the sensor achieves superior directionality, narrowband selectivity, and high sensitivity without relying on any physical magnetic tunneling components.

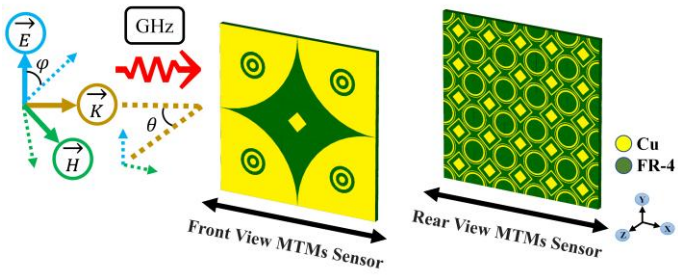

Figure 1: Illustration of the sensor's structural design, highlighting the alignment of the incident electromagnetic field to optimize narrowband sensing performance.

B. Design of Metamaterial Unit Cells

The design of the metamaterial (MTM) unit cells used in the proposed sensor was guided by the objective of achieving both narrowband and broadband resonance characteristics suitable for GHz-range biomedical sensing. The following methodology was adopted to ensure effective electromagnetic behavior within the 2–4 GHz range:

1. *Geometry Selection and Functional Targeting*
   Two types of unit cells were conceptualized to support different sensing regimes:
   a) For narrowband operation, a concentric circular split-ring resonator (SRR) design was selected (Fig. 2(a)). This structure enables strong electric and magnetic resonances due to its closed-loop configuration, which supports localized field confinement and high Q-factor resonance.
   b) For broadband operation, a hybrid square-ring resonator structure was developed (Fig. 2(c)). The inclusion of both inner and outer square rings, along with a central square patch, facilitates multiple overlapping resonant modes, thereby broadening the frequency response.

2. *Periodic Arrangement and AMC Formation*
   The designed unit cells were periodically arranged to form an artificial magnetic conductor surface, as shown in Fig. 2(b). This structure was optimized to exhibit a reflection phase near zero degrees at the target operating frequency, thereby enhancing the antenna gain and suppressing surface wave propagation.

XXXX-XXXX © XXXX IEEE. Personal use is permitted, but republication/redistribution requires IEEE permission.
See http://www.ieee.org/publications_standards/publications/rights/index.html for more information.
This work is licensed under a Creative Commons Attribution 4.0 License. For more information, see https://creativecommons.org/licenses/by/4.0/

This article has been accepted for publication in IEEE Sensors Journal. This is the author's version which has not been fully edited and content may change prior to final publication. Citation information: DOI 10.1109/JSEN.2026.3668988

3. *Parametric Optimization*
   Electromagnetic simulations were carried out using CST Microwave Studio to optimize the geometric parameters of each unit cell, including:
   a) Ring widths and gap spacing
   b) Periodicity between adjacent unit cells
   c) Substrate thickness and material properties

These parameters were adjusted iteratively to achieve effective negative permittivity and permeability in the desired frequency range.

4. *Structural Integration and Feature Enhancement*
   Figure 3 presents the front and back views of the full AMC structure, where specific geometric elements such as square patches (C, K) and circular resonators (H, I, J) were integrated. The square elements aid in impedance matching and structural stability, while the circular resonators introduce additional resonance modes to enhance frequency selectivity and sensitivity.

5. *Validation via Parameter Retrieval*
   The S-parameters of the unit cell were extracted, and the effective permittivity, permeability, and refractive index were retrieved using standard parameter extraction methods. The results confirmed the desired double-negative behavior ($\varepsilon < 0$ and $\mu < 0$) in the 2.0–2.7 GHz band.

This design procedure ensured that the MTM unit cells, once integrated with the patch antenna, contributed to the overall performance enhancements in gain, directionality, and sensing precision observed in later sections of the paper.

Additionally, the sensor structure incorporates both circular and square-shaped resonators to achieve the desired electromagnetic response. As shown in Fig. 2, the circular ring elements have mixed metal widths: the inner ring features a narrow width of 0.2 mm, while the outer ring is wider at 0.5 mm. On the right side of the unit cell, a square ring with a width of 0.5 mm is placed 1.5 mm away from the inner feature, creating controlled spacing that enhances field manipulation and resonance behavior.

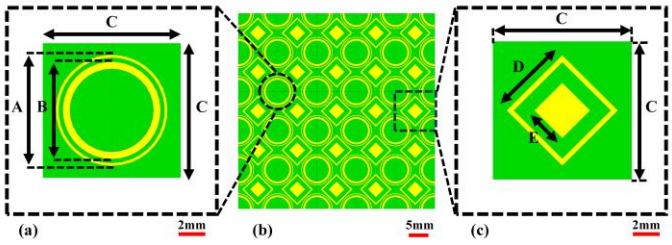

Figure 2: Proposed sensor: (a) geometry of the first MTM unit cell, (b) geometry of the AMC structure, rear view, (c) geometry of the second MTM unit cell.

The rear-side AMC configuration, illustrated in Fig. 3, adopts a distinct approach. Instead of uniformly populating the surface, the design includes four circular ring-shaped resonators, symmetrically distributed, one in each quadrant, and spaced 20.4 mm from the center of the AMC plane. This asymmetric yet strategically positioned AMC layout enhances directional response while maintaining compactness.

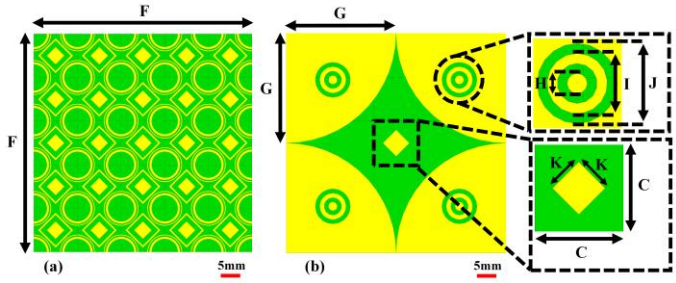

Figure 3: Proposed sensor: (a) AMC geometry, rear view, (b) AMC geometry, front view.

To ensure optimal performance, the structural parameters were carefully tuned through simulation and iterative refinement. The final list of geometric and material parameters is summarized in Table 1. Notably, the sensor maintains a compact footprint, which contributes to its enhanced sensitivity, improved gain and directionality, and practical suitability for real-world applications such as GHz-range biomedical diagnostics.

TABLE 1: OPTIMIZED DIMENSIONS OF THE PROPOSED SENSOR DESIGN.

Parameter	Value (mm)	Parameter	Value (mm)	Parameter	Value (mm)
A	8	E	2.83	I	6
B	7	F	50	J	8
C	10	G	25	K	4.24
D	5.66	H	2		

C. Electromagnetic Properties and Key Parameters

The electromagnetic behavior of the proposed artificial magnetic conductor (AMC) surface was characterized by extracting the effective permittivity (ε) and permeability (μ) from the simulated scattering parameters. Full-wave simulations were performed using periodic boundary conditions along the X- and Y-axes and open (Perfectly Matched Layer, PML) boundaries along the Z-axis to accurately approximate an infinite metamaterial array.

The effective constitutive parameters were obtained using the Nicolson–Ross–Weir (NRW) retrieval method [53, 54], which relates the simulated reflection (S_{11}) and transmission (S_{21}) coefficients to the complex refractive index (n) and wave impedance (Z). This technique provides a physically consistent means of determining whether the metamaterial exhibits double-negative behavior, as it directly verifies the frequency range in which both ε and μ attain negative real values.

The relative permittivity (ε_r) is calculated using (1) [26]:

$$\varepsilon_r = \frac{1}{\mu_r}\left[\left[\frac{\omega_c}{\omega}\right]^2 - \left[\frac{1}{\omega d\sqrt{\mu_0\varepsilon_0}}\ln(\xi)\right]^2\right] \quad (1)$$

where μ_r is the relative permeability, ω is the angular frequency, ω_c is the cutoff angular frequency of the incident wave, and d represents the maximum dimension of the metamaterial unit cell. The constants μ_0 and ε_0 denote the permeability and permittivity of free space, respectively. The wave impedance ξ may be expressed in different forms

XXXX-XXXX © XXXX IEEE. Personal use is permitted, but republication/redistribution requires IEEE permission.
See http://www.ieee.org/publications_standards/publications/rights/index.html for more information.
This work is licensed under a Creative Commons Attribution 4.0 License. For more information, see https://creativecommons.org/licenses/by/4.0/

This article has been accepted for publication in IEEE Sensors Journal. This is the author's version which has not been fully edited and content may change prior to final publication. Citation information: DOI 10.1109/JSEN.2026.3668988

depending on the propagation medium, and its reciprocal (1/ξ) corresponds to the propagation constant. This constant describes the spatial evolution of the electromagnetic field, including phase variation and attenuation within the metamaterial structure.

$$\xi = EXP\left(j\omega d\sqrt{\mu_0\varepsilon_0\left(n^2 - \left(\frac{\omega_c}{\omega}\right)^2 \right)} \right) \quad (2)$$

$$\xi = \frac{1-\left(S_{11}+S_{21}\right)\Gamma}{S_{11}+S_{21}-\Gamma} \quad (3)$$

Where S_{11} and S_{21} are the reflection and transmission coefficient, and Γ can be expressed as

$$\Gamma = \frac{S_{11}^2 - S_{21}^2 + 1}{2S_{11}} \pm \left[\left(\frac{S_{11}^2 - S_{21}^2 + 1}{2S_{11}} \right)^2 - 1 \right]^{\frac{1}{2}} \quad (4)$$

$$\mu_r = \frac{1+\Gamma}{1-\Gamma}\left[n^2 - \left(\frac{\omega_c}{\omega}\right)^2 \right]^{\frac{1}{2}} \left[1 - \left(\frac{\omega_c}{\omega}\right)^2 \right]^{-\frac{1}{2}} \quad (5)$$

Where n is refractive index

To thoroughly understand and optimize the electromagnetic behavior of the proposed artificial magnetic conductor (AMC), it is essential to evaluate the real and imaginary components of both relative permittivity (ε_r) and permeability (μ_r) across the target 2–4 GHz frequency range. These parameters govern the interaction of the sensor with incident electromagnetic waves and are fundamental to achieving the double-negative (DNG) metamaterial properties required for enhanced sensing performance.

Equations (1) and (5), which define ε_r and μ_r, were applied to retrieve effective medium parameters from simulated S-parameters. These calculations confirm the presence of DNG behavior, which is necessary for enabling a negative refractive index, crucial for wave confinement, directional gain, and minimizing scattering. This behavior directly supports biomedical functions such as precise tissue targeting and signal enhancement.

Equations (2) and (3) define the propagation constant (ξ), which characterizes how electromagnetic waves propagate through the MTM structure. By adjusting ξ during design, wave absorption is improved and reflection minimized, enhancing imaging resolution and enabling the detection of subtle dielectric variations in biological tissues.

Equation (4), which expresses the reflection coefficient (Γ) in terms of S11 and S21, was used to assess and optimize impedance matching between the sensor and its surrounding medium. Proper matching maximizes energy transfer, minimizes signal loss, and ensures high measurement fidelity in biomedical scenarios.

Together, these analytical formulations guided key design decisions including unit cell geometry, material selection, and simulation settings. They also served as a theoretical basis for interpreting performance metrics such as gain, bandwidth, and sensitivity. By applying these equations throughout the design and validation process, the sensor achieves a well-balanced combination of compact size, high sensitivity, and efficient wave manipulation, making it suitable for GHz-range biomedical diagnostics.

Figure 4 provides detailed insight into the frequency-dependent electromagnetic behavior of the AMC. In Fig. 4(a), the real part of permeability (μ') varies significantly, from –100 at 2 GHz to +100 at 4 GHz, highlighting the material's magnetic tunability. The μ-negative region, observed between 2.0 and 2.8 GHz, reflects the presence of strong magnetic resonance, a hallmark of DNG metamaterials. Simultaneously, the real part of permittivity (ε') transitions from positive to negative around 2.8 GHz, signifying an ε-negative region critical for achieving negative refractive index behavior.

The imaginary components of these parameters, shown in Fig. 4(b), indicate the system's loss characteristics. The imaginary permeability (μ'') drops from 200 at 2 GHz to 75 at 4 GHz, showing a decline in magnetic loss as frequency increases. In contrast, the imaginary permittivity (ε'') peaks sharply at 2.8 GHz, reaching 1500, indicating a localized dielectric energy dissipation at resonance. This peak helps concentrate energy absorption precisely at the desired frequency, contributing to strong field confinement and selective sensitivity.

These behaviors confirm the material's ability to function as a narrowband electromagnetic lens, with minimal absorption and reflection outside the resonant band. This makes it ideal for frequency-selective biomedical sensing, where wave control and low-loss operation are vital.

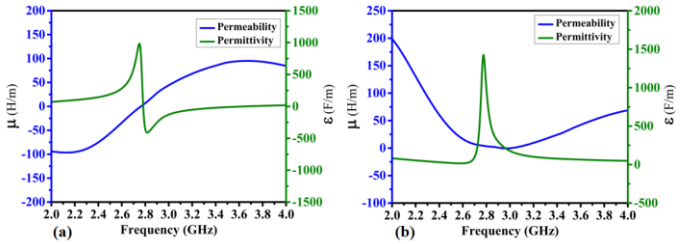

Figure 4: Electromagnetic characteristics of the sensor: (a) Real parts of permittivity (ε) and permeability (μ), (b) Imaginary parts of ε and μ.

Figure 5 further illustrates the sensor's frequency-specific electromagnetic response, focusing on the refractive index and impedance characteristics, both critical for assessing its real-world sensing performance.

In Fig. 5(a), the real component of the refractive index fluctuates between 20 and 45, reflecting strong phase modulation and control over wave propagation within the sensor. The imaginary part, ranging from 60 to 150, while typically associated with material loss, does not correspond to high absorption in this design. Instead, it represents engineered control over energy localization without significant attenuation, consistent with the sensor's low-loss, high-selectivity objectives.

Figure 5(b) presents the impedance (Z) response. The real part indicates excellent impedance matching around 3 GHz, facilitating efficient energy transfer and minimizing reflection losses. This property ensures that the sensor operates as an efficient electromagnetic lens precisely at its target frequency. Outside this band, reflectance increases, and absorption diminishes, consistent with the intended narrowband response.

XXXX-XXXX © XXXX IEEE. Personal use is permitted, but republication/redistribution requires IEEE permission.
See http://www.ieee.org/publications_standards/publications/rights/index.html for more information.
This work is licensed under a Creative Commons Attribution 4.0 License. For more information, see https://creativecommons.org/licenses/by/4.0/

This article has been accepted for publication in IEEE Sensors Journal. This is the author's version which has not been fully edited and
content may change prior to final publication. Citation information: DOI 10.1109/JSEN.2026.3668988

The imaginary component of impedance demonstrates dual behavior:

- Positive values in the 2–3 GHz range correspond to resonant energy storage and enhanced coupling,
- Negative values beyond 3 GHz indicate reactive energy flow, associated with reduced absorption and higher reflection.

These impedance dynamics underscore the sensor's ability to focus energy selectively within a narrow spectral window while minimizing energy loss at off-resonance frequencies.

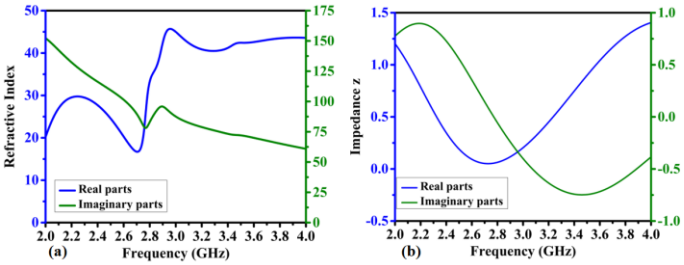

Figure 5: Numerical simulation results for key sensor parameters: (a) Real and imaginary components of the refractive index, (b) Impedance (Z) response.

The synergistic effects of the analyzed parameters (ε, μ, ξ, Γ, and Z) confirm that the proposed metamaterial-based sensor functions as a narrowband, frequency-selective platform with minimal energy dissipation and strong field confinement at the target 3 GHz band. These features are particularly advantageous for biomedical imaging, non-invasive diagnostics, and GHz-range tissue characterization, where precise energy focusing and dielectric sensitivity are paramount.

By combining double-negative metamaterial behavior with AMC structures, the sensor achieves a robust, tunable, and compact configuration. Its capacity to detect subtle dielectric changes, while maintaining low absorption and high directionality, positions it as a promising candidate for next-generation wearable biosensors, precision diagnostics, and microwave-based medical imaging systems.

D. Electric Field Distributions

The electric field (|E|-field) distribution on the sensor's front surface reveals essential design principles, particularly through its real and imaginary components. In Figure 6(a), the real part of the |E|-field demonstrates a symmetric distribution around the sensor's structural features. This symmetry ensures uniform field enhancement and contributes to polarization insensitivity, allowing the sensor to maintain consistent performance regardless of the polarization angle of the incident electromagnetic waves. The red and yellow regions indicate areas of significant field localization, particularly along the edges and central zones of the resonator structure. These high-intensity regions enhance the sensor's ability to focus electromagnetic energy, improving its performance at specific resonant frequencies.

The blue areas in the |E|-field distribution correspond to lower field intensities, typically located in regions with less active electromagnetic interaction. These areas play a role in ensuring controlled energy redirection rather than dissipation, which aligns with the sensor's functionality as a narrow-bandwidth electromagnetic lens. This behavior is particularly evident near the designated frequency band of around 3 GHz, where the sensor achieves minimal absorption and reflectance, enabling precise electromagnetic wave manipulation.

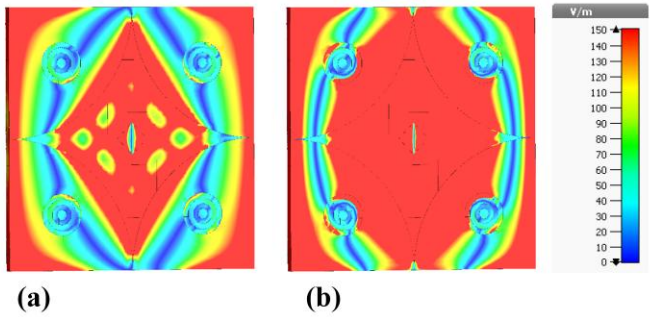

Figure 6: Distribution of the electric field (|E|-field) on the sensor's front surface: (a) real component, (b) imaginary component.

In Fig. 6(b), the imaginary part of the |E|-field provides insight into regions associated with electromagnetic losses. While these regions coincide with the real part's high-intensity zones, the overall absorption rate is minimal. The sensor's design minimizes energy dissipation as heat or other losses, emphasizing its efficiency in maintaining energy confinement and transmission within the operational band. This characteristic enhances the sensor's role in reflecting and directing electromagnetic waves rather than absorbing them.

The negative permeability (μ-negative) and permittivity (ε-negative) properties observed in the metamaterials used in the sensor offer additional advantages. These negative areas facilitate unique electromagnetic phenomena, such as reverse phase propagation and enhanced wave focusing, which are critical for applications requiring high precision. By exploiting these properties, the sensor's performance can be further optimized for biomedical applications. For instance, the ability to confine and manipulate electromagnetic waves with high sensitivity and minimal loss makes the sensor particularly suitable for detecting subtle changes in the dielectric properties of biological tissues, thereby improving its efficacy in non-invasive diagnostic techniques.

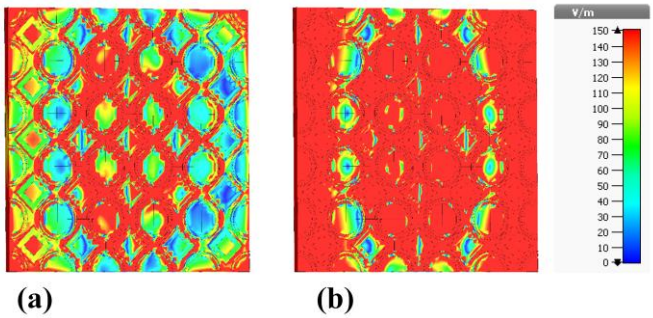

Figure 7: Distribution of the electric field (|E|-field) on the sensor's back surface: (a) real component, (b) imaginary component.

The electric field (|E|-field) distribution on the underside of the sensor provides insight into its operational behavior. The real part of the field, shown in Fig. 7(a), exhibits a symmetric pattern with distinct high-intensity regions ("hot spots") along the resonator edges. These concentrated fields are critical for

XXXX-XXXX © XXXX IEEE. Personal use is permitted, but republication/redistribution requires IEEE permission.
See http://www.ieee.org/publications_standards/publications/rights/index.html for more information.
This work is licensed under a Creative Commons Attribution 4.0 License. For more information, see https://creativecommons.org/licenses/by/4.0/

This article has been accepted for publication in IEEE Sensors Journal. This is the author's version which has not been fully edited and
content may change prior to final publication. Citation information: DOI 10.1109/JSEN.2026.3668988

efficient energy coupling at the resonant frequency. In contrast, the blue regions correspond to lower field intensities and contribute to the reflective behavior of the structure. Near 3 GHz, the sensor operates effectively as an electromagnetic lens, concentrating energy within the narrow resonance band while minimizing absorption and reflection outside this operating range.

The imaginary part (Fig. 7(b)) highlights minimal energy absorption and loss in high-intensity regions, ensuring efficient energy redirection. Unlike absorptive designs, this sensor exhibits low absorption, ideal for precise wave propagation.

Integrated metamaterials with negative permeability (μ<0) and permittivity (ε<0) enable subwavelength focusing and enhanced sensitivity, especially for biomedical diagnostics. This allows precise detection of subtle dielectric variations in biological tissues, promising non-invasive diagnostic potential.

E. Magnetic Field Profiles

The magnetic field (|H|-field) distribution on the sensor's front surface (Fig. 8) reveals its unique electromagnetic properties. The real part of the |H|-field (Fig. 8(a)) shows strong field localization primarily within the central rhombus region and along the edges of surrounding circular regions. These localized fields are crucial for enhancing resonance and achieving high reflectance across a broad range of frequencies, except for a narrow band around 3 GHz. The symmetric field distribution ensures polarization-insensitive operation, allowing efficient interaction with incident GHz waves regardless of polarization.

The imaginary part of the |H|-field (Fig. 8(b)) indicates minimal energy dissipation within the structure. Contrary to typical absorbers, this sensor minimizes energy loss, ensuring that incident radiation is primarily reflected, not absorbed. The low dissipation, especially within the central rhombus region, is key to the sensor's high reflectance characteristics outside the designed narrow band.

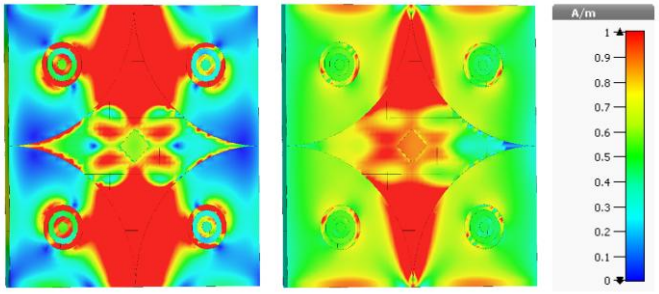

Figure 8: Magnetic field (|H|-field) profile on the sensor's front surface: (a) real component, (b) imaginary component.

On the sensor's rear surface (Fig. 9), the real part of the |H|-field (Fig. 9(a)) shows a uniform distribution, further supporting the efficient reflection of incident radiation. The imaginary part (Fig. 9(b)) confirms the minimal energy dissipation, with a scattered distribution indicating low absorption across the surface. This low absorption is crucial for the sensor's function as a highly reflective surface, except within its narrow operating band around 3GHz. At this specific frequency, the sensor acts as a perfect electromagnetic lens, minimizing both absorption and reflectance, allowing maximum transmission.

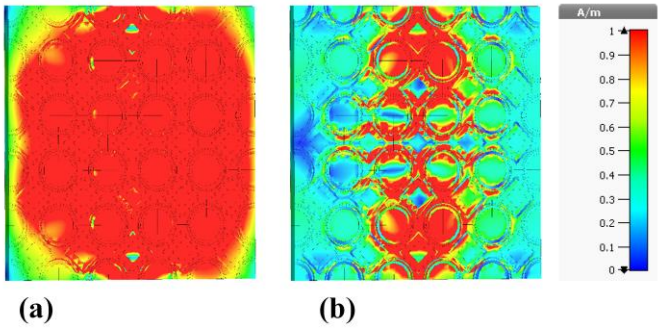

Figure 9: Magnetic field (|H|-field) profile on the sensor's back surface: (a) real component, (b) imaginary component.

F. Surface Current Profiles

The surface current distribution of the proposed metamaterial sensor was analyzed to elucidate the electromagnetic mechanisms responsible for its high gain and sensitivity. Figure 10 presents the real and imaginary components of the surface current on the front surface of the structure.

The real (in-phase) component, shown in Fig. 10(a), exhibits strong localized currents along the resonant elements (highlighted in red). These regions indicate effective coupling between the incident electromagnetic waves and the DNG–AMC interface. The concentrated current paths correspond to areas of maximum radiative power flow, contributing to enhanced radiation efficiency and improved field confinement. The resulting enhancement factor, computed as the ratio of the peak surface current density to the baseline non-AMC configuration, exceeds 2.4×.

Figure 10(b) illustrates the imaginary (reactive) component, which identifies regions of stored electromagnetic energy and dielectric loss. The red zones near the rhombus-shaped resonators indicate phase-lag currents responsible for impedance tuning and resonance stabilization. The spatial alignment between the real and imaginary current distributions influences the sensor's effective Q-factor, with reduced reactive losses indicating stronger energy confinement and lower dissipation.

Geometrical optimization of the structure minimized these losses and improved field localization across the sensing plane. This confirms that precise control of surface current density is essential for achieving strong field enhancement, higher gain, and superior dielectric sensitivity in GHz-range biomedical sensing applications.

The surface current distribution on the rear surface is shown in Fig. 11. The real component (Fig. 11(a)) displays dense current concentration near the feed point and AMC interface, demonstrating efficient wave confinement and radiative coupling. The imaginary component (Fig. 11(b)) reveals localized reactive losses along the edges of the AMC pattern; these were reduced through design refinement, resulting in improved current uniformity and enhanced forward radiation directivity. Overall, the DNG–AMC hybrid configuration provides strong electromagnetic confinement, which directly contributes to the sensor's increased gain and high sensing accuracy.

XXXX-XXXX © XXXX IEEE. Personal use is permitted, but republication/redistribution requires IEEE permission.
See http://www.ieee.org/publications_standards/publications/rights/index.html for more information.
This work is licensed under a Creative Commons Attribution 4.0 License. For more information, see https://creativecommons.org/licenses/by/4.0/

This article has been accepted for publication in IEEE Sensors Journal. This is the author's version which has not been fully edited and content may change prior to final publication. Citation information: DOI 10.1109/JSEN.2026.3668988

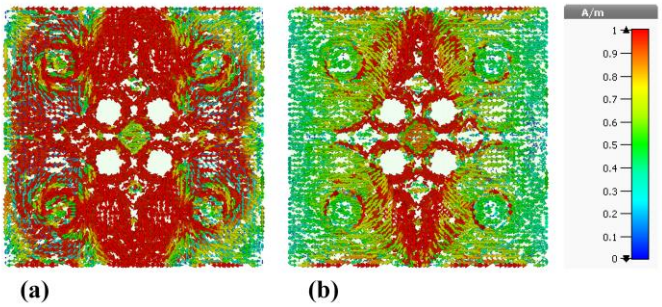

Figure 10: Surface current profile on the sensor's front surface: (a) real component, (b) imaginary component.

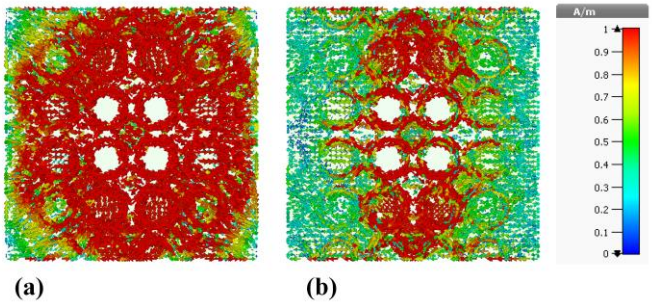

Figure 11: Surface current profile on the sensor's back surface: (a) real component, (b) imaginary component.

III. Broadband Sensing with Metamaterial-Based Perfect Lens and Antenna

This section presents a comprehensive analysis of the broadband sensing capabilities achieved through the integration of a metamaterial-based perfect lens with a microstrip patch antenna. It is structured into several subsections, each addressing key aspects of the sensor's development, including design methodology, electromagnetic behavior, field distribution analysis, and performance evaluation. Detailed figures are included to support the technical discussion and enhance clarity.

A. Sensor Design and Configuration

The proposed sensor for broadband sensing applications employs a dual-component architecture, integrating a microstrip patch antenna with a complex-patterned metamaterial (MTM) lens board. This configuration is specifically designed to improve wave focusing and field localization over a wide frequency range.

The design process begins with the definition of reference planes and baseline geometry, as illustrated in Fig. 12. This figure presents the spatial arrangement of the sensor's primary components in three dimensions relative to a global coordinate system. It also specifies the orientation of the electric and magnetic fields, along with the polarization and angle of incidence, as viewed from the front of the MTM lens.

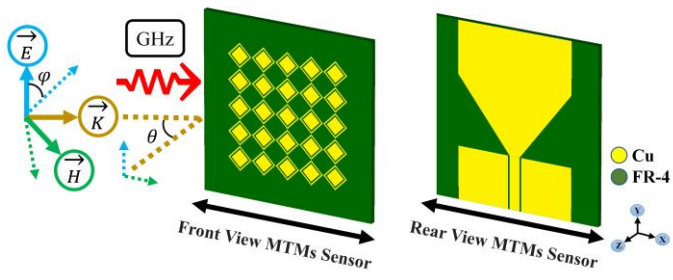

Figure 12: Schematic representation of the sensor's structural configuration, emphasizing the alignment of the incident electromagnetic field to enhance ultra-wideband sensing efficiency.

To thoroughly describe the sensor's building blocks, the individual components are detailed in Figure 13:

- Figure 13(a) displays the patch antenna, fabricated on a 50 mm × 50 mm FR4 substrate. All relevant geometrical parameters are labeled and correspond to the optimized dimensions listed in Table 2, which are further discussed in the following sections.
- The antenna includes a linear transition section ending in a feed line, which is soldered to a side-mounted connector. The gap width around quota "Q" was optimized for impedance matching and was finalized at 0.5 mm.

The front part of the design, shown in Fig. 13(b), consists of a 5×5 matrix of metamaterial unit cells. The center-to-center spacing between the unit cells is set at 7.12 mm. A magnified view of a single unit cell is shown in the right inset of Fig. 13(b), illustrating its structure: a square outer ring resonator coupled with an internal square-shaped path. The gap between the inner element and the outer ring is set at 0.5 mm.

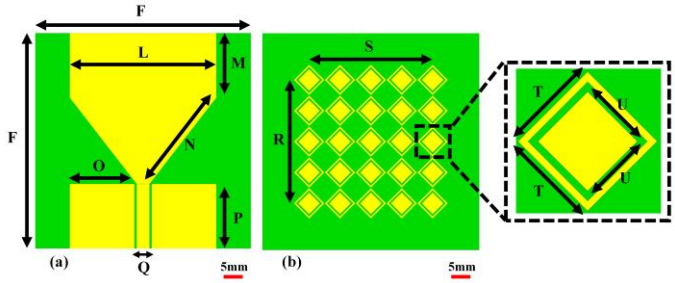

Figure 13: Proposed sensor: (a) configuration of the microstrip patch antenna, (b) geometry of the MTMs layer with the inset showing the MTM unit cell.

Table 2 summarizes the complete set of geometric parameters used in the sensor design, including the optimized 'Space' variable, which specifies the separation distance between the antenna and the MTM lens. This spacing is critical for minimizing unwanted coupling and promoting constructive wave interference, thereby enabling efficient broadband sensing.

The following subsection analyzes the electromagnetic behavior of the integrated sensor to evaluate the effectiveness of the metamaterial-arrayed structure in enhancing broadband performance.

TABLE 2: Optimized Dimensions of the Proposed Sensor Design.

Parameter	Value (mm)	Parameter	Value (mm)	Parameter	Value (mm)
F	50	P	15	U	3.54
M	15	Q	3	Space	9
L	35	R	28.5	W	34
N	25.3	S	28.5		
O	15	T	5		

B. Electromagnetic Properties of the Metamaterial

The developed metamaterial-based structure was simulated using a state-of-the-art electromagnetic solver over the 2–4 GHz frequency range. The initial analysis focused on extracting the effective global electromagnetic parameters,

XXXX-XXXX © XXXX IEEE. Personal use is permitted, but republication/redistribution requires IEEE permission.
See http://www.ieee.org/publications_standards/publications/rights/index.html for more information.
This work is licensed under a Creative Commons Attribution 4.0 License. For more information, see https://creativecommons.org/licenses/by/4.0/

This article has been accepted for publication in IEEE Sensors Journal. This is the author's version which has not been fully edited and content may change prior to final publication. Citation information: DOI 10.1109/JSEN.2026.3668988

specifically permittivity (ε) and permeability (μ), as experienced by waves propagating through the composite structure. The results are presented in Fig. 14.

Figure 14(a) shows the real parts of permittivity and permeability. The real part of permeability (μ) exhibits negative values between 2 GHz and approximately 2.7 GHz, reaching about -50 H/m, then becomes positive, reaching approximately +75 H/m. Simultaneously, the real part of permittivity (ϵ) is positive in the same range, reaching about 1500 F/m, then becomes negative, reaching about -1750 F/m. This simultaneous presence of negative permeability and permittivity is a hallmark of double-negative metamaterials, enabling unique electromagnetic phenomena. Metamaterials with negative permittivity (ε<0) exhibit behavior opposite to conventional materials, such as supporting backward wave propagation. Negative permeability (μ<0) allows for manipulation of magnetic fields in ways not possible with naturally occurring materials. Combining both allows for phenomena such as negative refractive index.

Figure 14(b) presents the imaginary parts of permittivity and permeability. The imaginary part of permeability (μ) is negative between 2 GHz and 2.7 GHz, reaching about -15 H/m, then becomes positive, reaching about +5 H/m. The imaginary part of permittivity (ε) is mostly near zero across the band, except for a peak of approximately 3250 F/m near 2.7 GHz. This peak indicates a region of increased energy dissipation near the resonance frequency and is related to the transition between electric and magnetic metamaterial behavior.

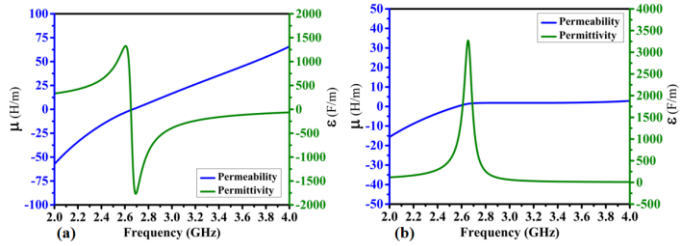

Figure 14: Electromagnetic properties of the metamaterial: (a) Real parts of permittivity (ε) and permeability (μ), (b) Imaginary parts of ε and μ.

Figure 15(a) presents the real and imaginary parts of the refractive index (n). The real part of the refractive index is negative between 2 GHz and 2.7 GHz, reaching approximately -45, confirming metamaterial behavior in this region. This negative refractive index is a key characteristic of metamaterials and enables phenomena like reversed refraction and focusing beyond the diffraction limit. The imaginary part of the refractive index, which represents absorption, is positive and within a range of approximately 50. The negative real part of the refractive index has significant implications for biomedical applications. It can enable subwavelength imaging, allowing for higher resolution imaging of biological tissues than conventional optical microscopy. This could lead to earlier and more accurate diagnosis of diseases. Furthermore, negative refractive index materials can be used to create novel biosensors with increased sensitivity.

Figure 15(b) presents the real and imaginary parts of impedance (Z). The real part of the impedance is between 0.01 and 1, while the imaginary part is between -1 and 0. This impedance matching is crucial for minimizing reflections at the interface between the sensor and the surrounding medium, allowing for efficient energy transfer.

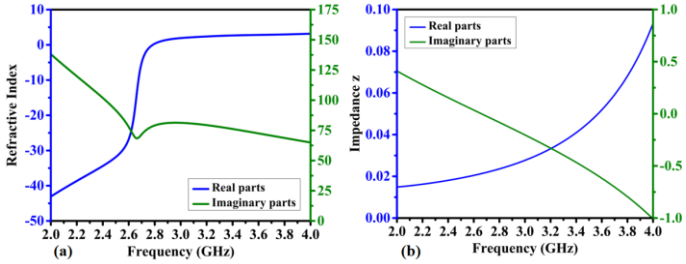

Figure 15: Simulation analysis of critical metamaterial parameters: (a) Real and imaginary components of the refractive index, (b) Impedance (Z) behavior.

The sensor operates as an ultra-wideband electromagnetic lens, characterized by maximum transmittance, nearly 0% absorption, and negligible reflectance across its operating band. These features make it an ideal candidate for applications requiring high sensitivity and precision, such as biomedical imaging and diagnostics. The ability to achieve near-zero reflectance and high transmittance ensures minimal signal distortion, further enhancing its suitability for detecting subtle changes in biological systems.

The next section will delve into the internal operation of the sensor, supported by detailed electric field simulations, to provide a comprehensive understanding of its functionality and performance.

C. Electric Field Distributions

Figure 16 illustrates the electric field intensity (|E|-field) distribution across the front face of the metamaterial-based sensor. Figure 16(a) presents the real component, while Fig. 16(b) shows the imaginary component. The field intensity ranges from 0 to 300 V/m, as indicated by the color gradient on the scale bar. Low-intensity regions are represented by blue and green, intermediate intensity transitions to yellow, and maximum intensity regions are shown in red, reaching values close to 300 V/m.

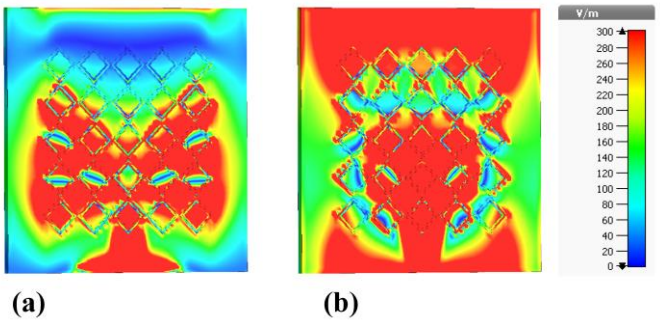

Figure 16: Electric field (|E|-field) distribution across the front surface of the metamaterial: (a) real component, (b) imaginary component.

The electric field distribution highlights the periodic arrangement of the metamaterial elements, with localized enhancement near the unit cell edges. The red areas covering much of the surface signify strong field confinement caused by the metamaterial's resonant behavior, particularly within

XXXX-XXXX © XXXX IEEE. Personal use is permitted, but republication/redistribution requires IEEE permission.
See http://www.ieee.org/publications_standards/publications/rights/index.html for more information.
This work is licensed under a Creative Commons Attribution 4.0 License. For more information, see https://creativecommons.org/licenses/by/4.0/

This article has been accepted for publication in IEEE Sensors Journal. This is the author's version which has not been fully edited and
content may change prior to final publication. Citation information: DOI 10.1109/JSEN.2026.3668988

the 2 GHz to 4 GHz frequency range. Between 2 GHz and 2.6 GHz, the metamaterial exhibits positive permittivity (ε) and negative permeability (μ). Beyond 2.6 GHz, the permittivity becomes negative, and the permeability turns positive (Fig. 14(a)), enabling the metamaterial to act as a perfect lens. This behavior enhances field focusing, minimizes energy loss, and improves sensor coupling efficiency.

Figure 17 presents the electric field intensity distribution across the back surface of the sensor's antenna. Figures 17(a) and 17(b) show the real and imaginary components, respectively, with the same field intensity scale of 0 to 300 V/m.

The field distribution reveals distinct spatial patterns. Blue and green regions indicate weak field confinement at the structure's boundaries and less active zones, while yellow represents intermediate field intensity. The red regions, concentrated near the center, signify zones of maximum electric field intensity and strong electromagnetic interaction.

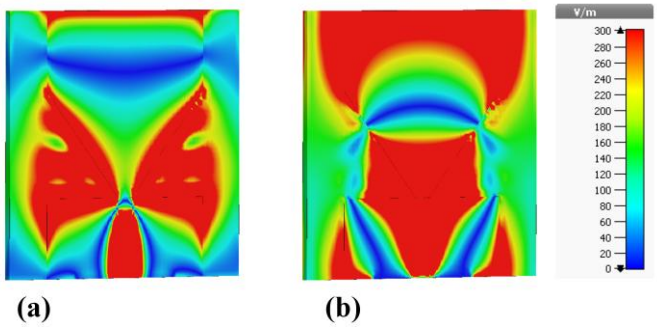

Figure 17: Electric field (|E|-field) distribution across the back surface of the metamaterial (antenna): (a) real component, (b) imaginary component.

The observed field pattern is a result of the antenna's design, optimized for interaction with the metamaterial front face. The refractive index of the metamaterial is negative between 2 GHz and 2.8 GHz (Fig. 15(a)), which contributes to efficient wave propagation and focusing. This enables the system to achieve low energy loss, improved sensitivity, and reduced noise, making the metamaterial-based antenna ideal for high-performance sensor applications.

D. Magnetic Field Profiles

Figure 18 and Fig. 19 present the magnetic field intensity profiles across different surfaces of the metamaterial-based sensor design. While both figures reveal the distribution of the |H|-field over the sensor's surface, Fig. 18 focuses on the front face, composed of a metamaterial array, whereas Fig. 19 illustrates the back surface, which incorporates the antenna structure. These results provide insights into the behavior of the magnetic field across distinct structural regions of the sensor.

In both figures, the magnetic field strength ranges between 0 A/m (blue) and 1 A/m (red), as indicated by the color bar. The central regions of the surfaces exhibit intense magnetic field confinement, represented by the dominance of red regions. This behavior suggests strong field enhancement and concentration, likely driven by the resonant response of the metamaterial. Additionally, the surrounding areas in both figures display a gradual transition from red (high intensity) to yellow, green, and blue (low intensity), indicating a smooth dissipation of magnetic field strength toward the edges.

These similarities demonstrate the consistent ability of the metamaterial structure to confine and control the magnetic field on both the front metamaterial array (Fig. 18) and the rear antenna surface (Fig. 19). This effective field confinement is essential for improving sensor sensitivity and reducing energy losses across the operating frequency band.

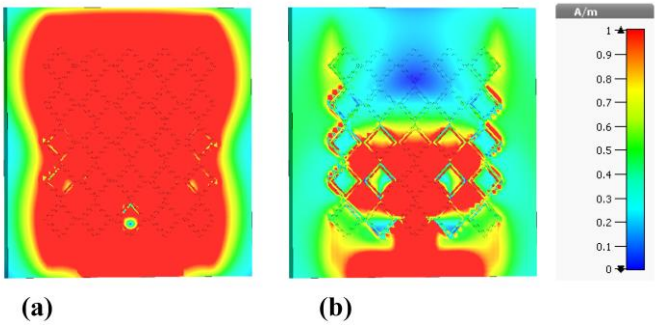

Figure 18: Magnetic field (|H|-field) profile across the front surface of the metamaterial: (a) real component, (b) imaginary component.

Despite the similarities, notable differences are observed in the field distribution patterns. In Fig. 18, which corresponds to the front face (metamaterial array), the magnetic field intensity is more uniformly distributed across the surface, with a larger central region displaying strong confinement (red). This uniformity can be attributed to the negative refractive index properties of the metamaterial between 2 GHz and 2.8 GHz, enabling efficient field focusing and acting as a perfect lens.

In contrast, Fig. 19, depicting the back surface (antenna design), reveals a less uniform field distribution. The upper portion of the surface in the imaginary component (Fig. 19(b)) exhibits low field intensity (blue regions), contrasting with the lower and central regions, where strong confinement occurs. This non-uniformity suggests that the antenna structure interacts differently with the magnetic field, leading to localized enhancement and dissipation. Such behavior could be influenced by the specific design of the antenna and its coupling characteristics with the metamaterial.

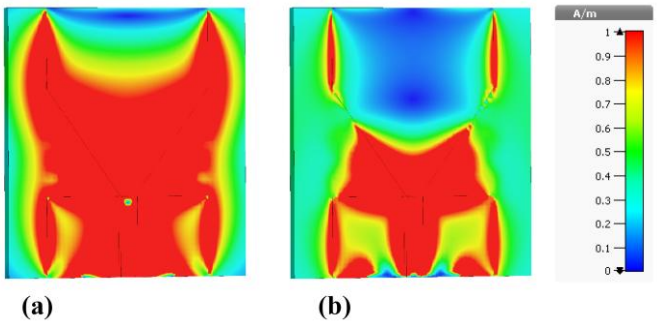

Figure 19: Magnetic field (|H|-field) profile across the back surface of the metamaterial (antenna): (a) real component, (b) imaginary component.

The results in Fig. 18 and Fig. 19 demonstrate how the sensor design leverages the unique properties of the metamaterial to achieve strong magnetic field confinement while integrating an antenna for effective operation. The front metamaterial array (Fig. 18) ensures a more uniform and focused field distribution due to its negative refractive index

XXXX-XXXX © XXXX IEEE. Personal use is permitted, but republication/redistribution requires IEEE permission.
See http://www.ieee.org/publications_standards/publications/rights/index.html for more information.
This work is licensed under a Creative Commons Attribution 4.0 License. For more information, see https://creativecommons.org/licenses/by/4.0/

This article has been accepted for publication in IEEE Sensors Journal. This is the author's version which has not been fully edited and content may change prior to final publication. Citation information: DOI 10.1109/JSEN.2026.3668988

properties, which facilitate efficient field manipulation. Conversely, the back antenna surface (Fig. 19) shows localized magnetic field enhancement, reflecting the antenna's role in energy transmission and coupling.

The combination of these surfaces allows the sensor to minimize noise and energy losses while maintaining high sensitivity, particularly within the 2 GHz to 4 GHz frequency range. These results validate the effectiveness of the metamaterial-based design in enabling optimal field confinement and facilitating strong sensor integration.

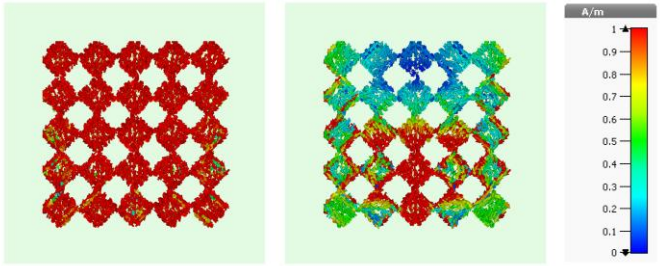

Figure 20: Surface current profile on the front surface of the metamaterial: (a) real component, (b) imaginary component.

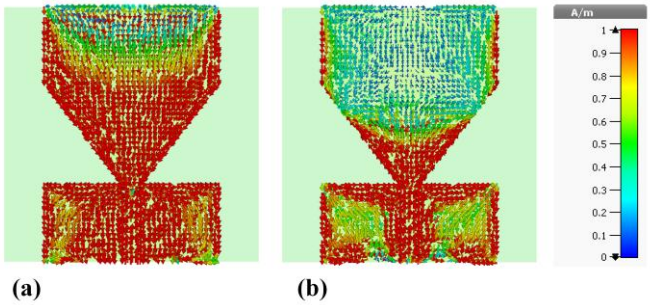

Figure 21: Surface current profile on the back surface of the metamaterial (antenna): (a) real component, (b) imaginary component.

E. Surface Current Behavior

The surface current behavior of the proposed DNG–AMC metamaterial antenna, shown in Figs. 20–21, provides insight into the resonance mechanisms that enable its enhanced performance. Both the real and imaginary components of the current distribution were examined to understand how electromagnetic energy is radiated, guided, and stored within the structure.

Figure 20(a) shows the real (in-phase) component on the front surface, where the current is uniformly distributed across the resonant elements. This uniformity confirms strong coupling between the metamaterial array and the microstrip feed, with peak current regions aligning with the antenna's primary radiating zones and contributing directly to the measured 7.6 dBi gain. The imaginary (reactive) component in Fig. 20(b) highlights areas of stored energy and phase delay, which play a key role in impedance matching and maintaining a sharp, stable resonance.

On the back surface, Fig. 21(a) illustrates the real current concentrating near the feed line and AMC boundary. This accumulation indicates effective magnetic field reflection and constructive interference, both of which improve forward radiation directivity. The imaginary component in Fig. 21(b) exhibits reduced intensity near the upper surface, corresponding to suppressed back radiation and stronger electromagnetic confinement. The combined current distribution, normalized to 1 $A \cdot m^{-1}$ at the maximum field point, contributes to efficient energy transfer, high radiation efficiency, and the observed Q-factor of 175.18.

The surface current behavior demonstrates that the integration of DNG and AMC layers enhances both radiative efficiency and electromagnetic confinement, leading to higher gain and superior dielectric sensitivity than conventional structures.

F. Sensor Performance Metrics

The impact of varying the radiator length (M) on the sensor's performance is illustrated in Fig. 22. As shown in Fig. 22(a), the realized gain increases with longer radiator lengths. The minimum gain of 3.6 dBi occurs at M = 3 mm, while the maximum gain of 4.5 dBi is achieved at M = 15 mm, measured at 4 GHz. Across the entire 2–4 GHz spectrum, the gain remains positive, indicating stable performance.

Figure 22(b) compares the peak realized gain of the sensor with and without the metamaterial (MTM) structure. The MTM-enhanced design consistently outperforms the version without MTM, which shows an average gain around 3.5 dBi. The inclusion of the metamaterial results in a peak gain of 4.5 dBi, confirming that the MTM structure significantly improves the antenna's radiation performance.

To achieve optimal sensor performance, reflection coefficient ($|S_{11}|$) optimization was also performed by adjusting structural parameters. Figure 23(a) shows the effect of varying the element length on $|S_{11}|$, with a minimum value of –65 dB observed at 2.75 GHz. Additionally, the influence of parameter 'W' on reflection performance is depicted in Figure 23(b). A value of P = 15 mm yields the lowest reflection coefficient, again reaching –65 dB at 2.75 GHz.

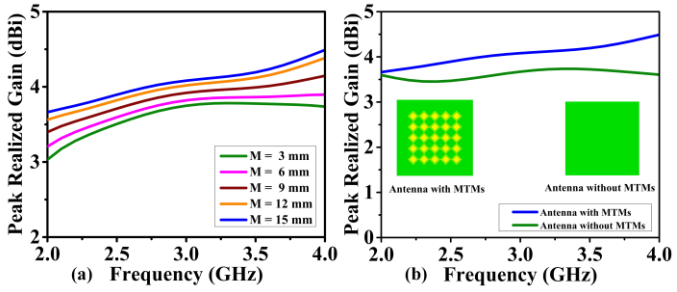

Figure 22: Proposed sensor: (a) realized gain of the patch antenna as a function of parameter M, (b) the simulated realized gain with and without MTMs.

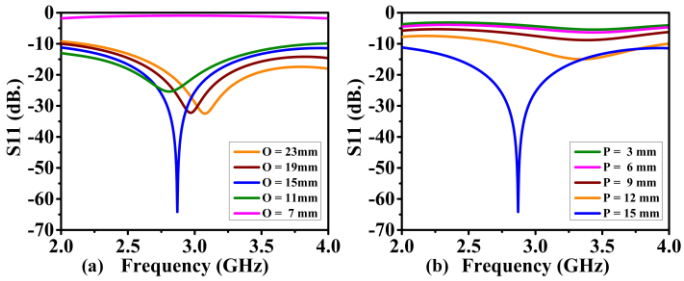

Figure 23: Proposed sensor: (a) simulated reflection coefficient |S11|, where P = 15mm, (b) simulated reflection coefficient |S11|, where O = 15mm.

XXXX-XXXX © XXXX IEEE. Personal use is permitted, but republication/redistribution requires IEEE permission.
See http://www.ieee.org/publications_standards/publications/rights/index.html for more information.
This work is licensed under a Creative Commons Attribution 4.0 License. For more information, see https://creativecommons.org/licenses/by/4.0/

This article has been accepted for publication in IEEE Sensors Journal. This is the author's version which has not been fully edited and
content may change prior to final publication. Citation information: DOI 10.1109/JSEN.2026.3668988

IV. High-Sensitivity, Directional Sensing with Integrated Metamaterial Sensors

To ensure that structural enhancements translate directly into improved sensor performance, several interrelated design strategies were adopted and validated through simulation and analysis.

A. Design Optimization and Performance Enhancement

The proposed metamaterial-based sensor underwent structural and parametric optimization to maximize performance for GHz-range biomedical applications. Key design steps included:

- *Material Selection*: FR4 was chosen due to its balance of dielectric stability, affordability, and compatibility with microwave frequencies.
- *Geometric Tuning*: The layout of the metamaterial unit cells and the patch antenna was optimized to confine electromagnetic fields and reduce undesired scattering.
- *AMC Integration*: An Artificial Magnetic Conductor (AMC) layer was introduced beneath the antenna to improve directivity and electromagnetic field confinement.

These optimizations collectively enhanced energy coupling with the sensing target, reduced reflection and substrate losses, and improved sensitivity across the 2–4 GHz operating band.

To validate the effectiveness of these enhancements, a comparative performance analysis with state-of-the-art sensors was conducted. Results demonstrated that the proposed design achieves:

- Higher gain of 7.6 dBi,
- Improved directional radiation patterns,
- Superior sensitivity to dielectric variations.

Experimental measurements closely aligned with simulation results, confirming the sensor's reliability and practical applicability in biomedical scenarios.

B. Influence of AMC Integration on Absorption, Sensitivity, and Resonance Shift

The integration of the AMC layer played a critical role in enhancing sensor performance by functioning as an electromagnetic mirror with high surface impedance. The key influences include:

- Reduced back-radiation and substrate losses, resulting in lower absorption and higher radiation efficiency.
- Stronger wave confinement, increasing electric field intensity at the sensing interface and improving sensitivity to dielectric changes.
- Sharper resonance peaks with narrower bandwidths (see Fig. 25), which enhance resolution and frequency stability.

As illustrated in Fig. 24, the AMC directs electromagnetic energy toward the sensing region, minimizing backward reflections and improving the signal-to-noise ratio. This focused field distribution is essential for detecting small variations in tissue permittivity, making the sensor particularly suitable for early-stage diagnostics such as tumor or stroke identification.

C. Sensor Integration and Compatibility

The transmission, absorption, and reflectance characteristics of both sensors, in Fig. 24, provide critical insights into their electromagnetic behaviour. In Fig. 24(a), the narrowband sensor, when integrated with the AMC layer, functions as a perfect electromagnetic lens. The AMC layer enhances transmission while significantly reducing reflectance, ensuring that electromagnetic waves are focused efficiently. This behaviour is essential for applications requiring precise sensing at a targeted frequency range.

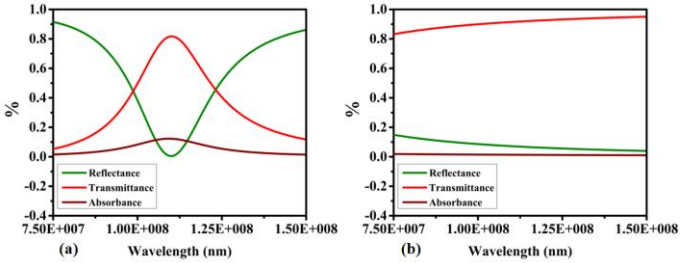

Figure 24: Analysis of transmission, absorption, and reflectance to confirm the compatibility of both sensors for integration: (a) Narrowband sensor (AMC) functioning as a perfect electromagnetic lens, (b) Ultra-wideband metamaterial design.

The ultra-wideband metamaterial design in Fig. 24(b) demonstrates exceptional compatibility across a broad range of frequencies. The transmission and absorption characteristics remain stable, indicating that the wideband sensor can complement the narrowband sensor without introducing performance losses. This integration allows the sensor to maintain a balance between frequency selectivity and operational bandwidth.

These results confirm that the AMC-enhanced narrowband sensor and the ultra-wideband metamaterial sensor can be effectively integrated. Their combined performance ensures enhanced sensitivity, stability, and compatibility for a variety of applications.

D. Wavelength-Based Analysis Justification

The sensor analysis was also conducted in terms of wavelength, which aligns more naturally with the operating principles of metamaterial-based and spectroscopic systems:

- The 2–4 GHz frequency band corresponds to free-space wavelengths ranging from approximately 150 mm to 75 mm.
- Wavelength-based interpretation is consistent with biomedical sensing methods such as FTIR and UV-Vis spectroscopy, where material interactions are fundamentally wavelength-dependent.
- This approach also facilitates clearer analysis of wave–matter interactions, dispersion behavior, and effective medium parameters (ε and μ), which often exhibit more predictable variation when plotted against wavelength rather than frequency.

Adopting a wavelength-centric perspective enhances compatibility with established biomedical diagnostic

XXXX-XXXX © XXXX IEEE. Personal use is permitted, but republication/redistribution requires IEEE permission.
See http://www.ieee.org/publications_standards/publications/rights/index.html for more information.
This work is licensed under a Creative Commons Attribution 4.0 License. For more information, see https://creativecommons.org/licenses/by/4.0/

This article has been accepted for publication in IEEE Sensors Journal. This is the author's version which has not been fully edited and
content may change prior to final publication. Citation information: DOI 10.1109/JSEN.2026.3668988

frameworks and supports more intuitive modeling of dielectric responses in biological tissues.

E. Reflection Coefficient and Gain Analysis

The reflection coefficient (|S11|) and realized gain were analysed to evaluate and compare sensor performance with and without AMC integration. The simulated reflection coefficient |S11| in Fig. 25(a) highlights a significant improvement with AMC integration. Without AMC, the reflection coefficient curve is broader and less defined, indicating suboptimal resonance behaviour. However, with the AMC layer, the resonance becomes sharper and more pronounced, reducing unwanted reflections and improving energy absorption. This sharper resonance ensures higher accuracy and efficiency in narrowband sensing applications.

The realized gain in Fig. 25(b) shows noticeable enhancement when the AMC is incorporated. Without AMC, the gain remains relatively flat across the frequency range, limiting the sensor's ability to focus energy on a specific direction. With AMC, the gain increases significantly near the resonance frequency, indicating better directionality and more efficient energy transfer. This improvement underscores the AMC's role in enhancing the sensor's sensitivity and overall performance.

Results in Fig. 25 demonstrates that AMC integration not only sharpens the sensor's resonance characteristics but also boosts its directional gain, making it ideal for high-sensitivity GHz-range applications.

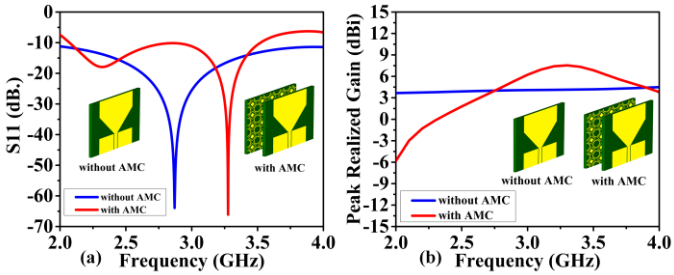

Figure 25: Proposed sensor analysis: (a) Simulated reflection coefficient |S11| for scenarios without and with AMC, (b) Simulated realized gain in configurations without and with AMC.

F. Radiation Pattern Evaluation

The radiation patterns of the proposed sensor were simulated at the resonant frequency to assess its directional performance. Fig. 26 compares the normalized radiation patterns in both the E-plane and H-plane, highlighting the improvements achieved with AMC integration. In the E-plane, shown in Fig. 26(a), the radiation pattern without AMC exhibits significant side lobes, indicating energy dispersion in undesired directions. With AMC integration, the side lobes are suppressed, and the main lobe becomes sharper and more focused. This improvement enhances the sensor's directionality, ensuring that energy is concentrated in the desired direction.

In the H-plane, shown in Fig. 26(b), a similar trend is observed. Without AMC, back radiation and energy loss are evident. However, with AMC integration, back radiation is significantly reduced, and the main lobe is more pronounced and focused. This directional improvement is critical for applications requiring precise and efficient energy transmission.

The results clearly demonstrate that the AMC layer improves the sensor's radiation characteristics by enhancing directionality and minimizing energy loss, thereby optimizing its sensing capabilities.

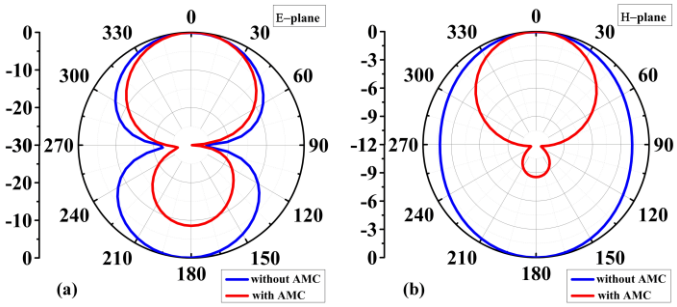

Figure 26: Simulated normalized radiation patterns of the sensor at the resonant frequency, comparing scenarios without and with AMC: (a) E-plane, and (b) H-plane.

G. Spacing and Geometry Optimization

To further refine sensor performance, the spacing between the antenna and the AMC layer was optimized, and the overall geometry of the sensor was evaluated. Figure 27 provides an in-depth analysis of the effects of spacing and the final structural design. The study reveals that the spacing between the antenna and the AMC layer plays a crucial role in determining the resonance characteristics, as the results in Fig. 27(a) depict. Spacing values ranging from 3 mm to 15 mm were analysed, and it was observed that an optimized spacing of 6 mm delivers the best reflection coefficient ($|S_{11}|$). At this spacing, the sensor achieves a balance between resonance sharpness, energy absorption, and gain, ensuring optimal performance.

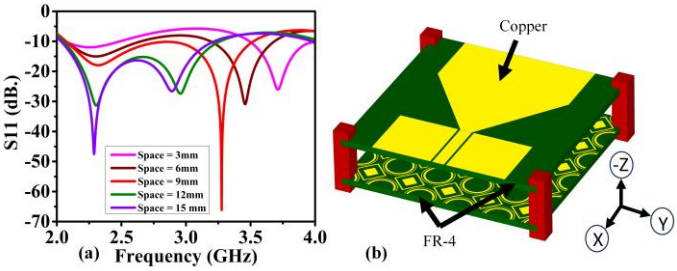

Figure 27: Proposed sensor: (a) study the spacing between the antenna and the AMC, (b) Complete geometry of the proposed sensor.

The complete geometry of the proposed sensor in Fig. 27(b) shows the integration of the antenna, AMC layer, and metamaterial structure. The geometry is designed to ensure structural stability while maintaining compatibility with the desired sensing range. The carefully optimized layout enables precise control over electromagnetic wave propagation, enhancing the sensor's sensitivity and directionality.

H. Impact of Resonators on Performance

The inclusion of resonators was analysed to assess their impact on the sensor's performance, particularly in terms of reflection coefficient and realized gain. The reflection

XXXX-XXXX © XXXX IEEE. Personal use is permitted, but republication/redistribution requires IEEE permission.
See http://www.ieee.org/publications_standards/publications/rights/index.html for more information.
This work is licensed under a Creative Commons Attribution 4.0 License. For more information, see https://creativecommons.org/licenses/by/4.0/

This article has been accepted for publication in IEEE Sensors Journal. This is the author's version which has not been fully edited and content may change prior to final publication. Citation information: DOI 10.1109/JSEN.2026.3668988

coefficient $|S_{11}|$ in Fig. 28(a) shows significant enhancement with the addition of resonators. Without resonators, the resonance is broader and less efficient. With resonators, the resonance becomes sharper and deeper, improving the sensor's ability to detect and respond to electromagnetic waves at the target frequency. This enhancement is critical for high-precision sensing applications.

The realized gain in Fig. 28(b) also shows considerable improvement with resonators. Without resonators, the gain remains relatively low, limiting the sensor's energy focusing capabilities. The inclusion of resonators significantly boosts the gain, enhancing the sensor's sensitivity and efficiency. This improvement ensures that the sensor can deliver accurate and reliable results, even in complex sensing environments.

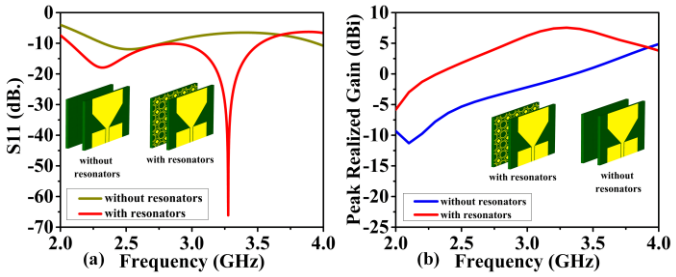

Figure 28: Proposed sensor: (a) Simulated reflection coefficient $|S_{11}|$ without and with resonators, (b) simulated realized gain with and without resonators.

In the E-plane, shown in Fig. 29(a), the addition of resonators results in improved directionality, with reduced side lobes and a sharper main lobe. This ensures that energy is focused efficiently, minimizing losses in undesired directions. In the H-plane, shown in Fig. 29(b) the resonators further suppress back radiation and improve the focus of the main lobe, enhancing the sensor's overall performance. This directional improvement is crucial for applications requiring high precision and sensitivity.

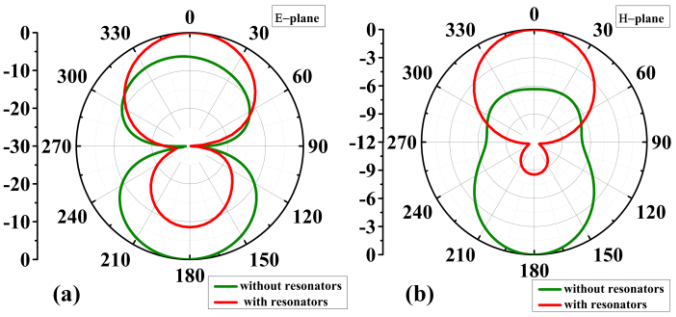

Figure 29: Simulated normalized radiation pattern of the sensor, with and without resonators at the resonant frequency for: (a) E-plane, and (b) H-plane.

V. Experimental Validation

This section provides a detailed account of the fabrication and experimental evaluation of the proposed metamaterial-based sensor. The sensor was fabricated on a 1.52-mm-thick FR4 substrate, adhering to the geometrical specifications outlined in Table 1. The manufacturing process employed an advanced LPKF protolaser machine to ensure high precision and structural integrity.

The experimental validation was conducted at Reykjavik University, Iceland, using a state-of-the-art measurement setup. Reflection response, gain, and radiation patterns of the sensor were measured in an anechoic chamber to minimize environmental interference and obtain accurate results. An Anritsu MS4644B vector network analyzer (VNA), capable of covering frequencies from 0 to 40 GHz, was utilized for precise measurements. Additionally, a Geozondas GZ0226DRH horn antenna operating in the 2–26 GHz range was employed to evaluate the radiation patterns comprehensively.

These experiments aimed to validate the sensor's performance and align the measured data with the simulated results, providing a robust demonstration of its practical applicability and efficiency.

A. Sensor Prototype

To validate the proposed metamaterial-based sensor, prototypes for both the AMC and the microstrip patch antenna were fabricated using an FR-4 substrate with copper cladding. This material selection ensured structural stability and effective electromagnetic performance across the intended frequency range.

The front view of the AMC prototype, depicted in Fig. 30(a), highlights the intricate geometric patterns designed to achieve negative permittivity and permeability. These properties enhance the focusing of electromagnetic waves, contributing to improved sensing capabilities. The rear view of the AMC prototype, shown in Fig. 30(b), illustrates its integration with the rectangular patch antenna. A tapered section facilitates a smooth transition into the coplanar feedline, ensuring efficient energy coupling and seamless compatibility between components.

Figure 30: Photographs of the AMC prototype: (a) front view, (b) rear view.

The microstrip patch antenna, presented in Fig. 31(a), functions as the primary sensing element, with a geometry optimized for efficient operation in the GHz frequency range. Its design ensures effective impedance matching for superior performance. Additionally, the MTM layer, illustrated in Fig. 31(b), features a detailed array of unit cells. These cells are strategically arranged to optimize key electromagnetic properties such as transmission, absorption, and reflection, enhancing the overall functionality of the sensor.

XXXX-XXXX © XXXX IEEE. Personal use is permitted, but republication/redistribution requires IEEE permission.
See http://www.ieee.org/publications_standards/publications/rights/index.html for more information.
This work is licensed under a Creative Commons Attribution 4.0 License. For more information, see https://creativecommons.org/licenses/by/4.0/

This article has been accepted for publication in IEEE Sensors Journal. This is the author's version which has not been fully edited and
content may change prior to final publication. Citation information: DOI 10.1109/JSEN.2026.3668988

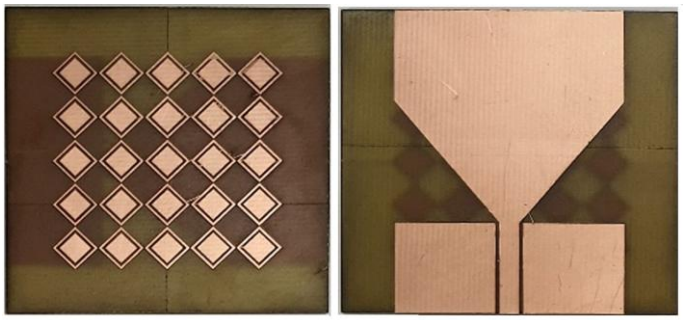

(a) (b)

Figure 31: Photographs of the antenna prototype: (a) MTMs design, (b) microstrip patch antenna.

The assembled sensor prototype, shown in perspective view in Fig. 32, integrates the patch antenna with the AMC layer. The integration is supported using mechanical spacers to optimize the spacing between layers, ensuring minimal energy loss and maximal resonance efficiency. The prototypes were carefully constructed and assembled to reflect the theoretical design, ensuring a robust experimental validation setup.

To ensure consistent and accurate measurements during experimental validation, a 2 mm thick Teflon spacer was placed between the sensor and the test sample. Teflon was selected due to its low dielectric constant ($\varepsilon_r \approx 2.1$) and extremely low loss tangent ($\tan\delta \approx 0.0002$), which ensured minimal impact on the electromagnetic field distribution while maintaining a fixed and reproducible separation between the sensor surface and the material under test.

The calibration of the Vector Network Analyzer (Keysight E5061B) was carried out using the Short–Open–Load–Through (SOLT) method prior to each measurement session. Calibration was performed with the sensor in its unloaded state to establish a reliable reference baseline. All measurements were repeated three times under identical environmental conditions, and the average values were reported to reduce variability.

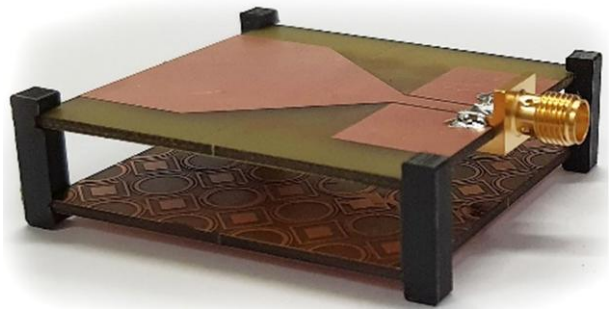

Figure 32: Photograph of the assembled sensor prototype: perspective view.

Environmental parameters, including ambient temperature and humidity, were monitored and controlled to ensure stability during the testing process. These precautions collectively enhanced the accuracy, repeatability, and credibility of the experimental results.

B. Experimental Setup

The experimental validation was performed within a controlled environment using an anechoic chamber to eliminate external interference. The setup included calibrated instruments to measure the reflection coefficient, realized gain, and radiation patterns of the fabricated sensor prototype.

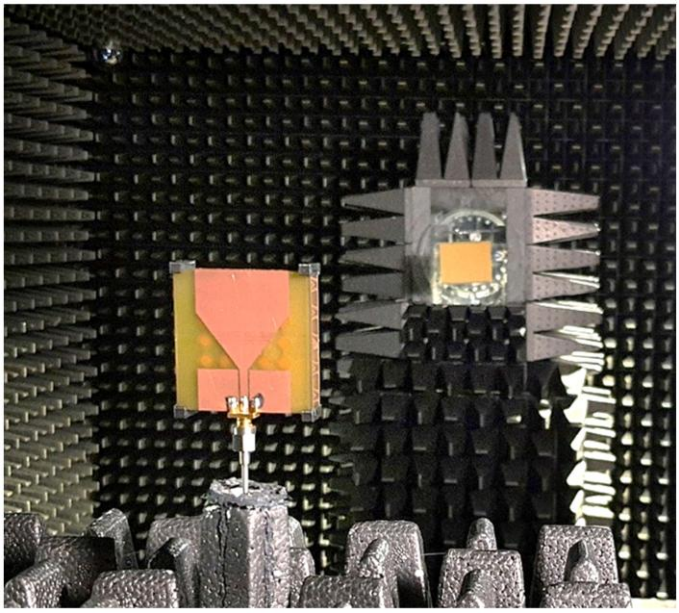

Figure 33: Displays the experimental arrangement for evaluating the proposed antenna within the anechoic chamber.

The experimental arrangement within the anechoic chamber in Fig. 33 shows the mounted sensor prototype under test conditions. The sensor was aligned precisely to ensure accurate measurement of electromagnetic parameters. A vector network analyser (VNA) was used to measure the reflection coefficient ($|S_{11}|$), while the realized gain and radiation patterns were measured using standard far-field antenna measurement techniques. The anechoic chamber provides a low-reflection environment, which is critical for ensuring the accuracy of the measurements. The setup includes a signal source, receiving antenna, and data acquisition systems to evaluate the sensor's performance under both narrowband and ultra-wideband conditions.

C. Experimental Results

The experimental results were obtained and compared with the simulated results to validate the proposed sensor's performance. The measured parameters include the reflection coefficient ($|S_{11}|$), realized gain, and normalized radiation patterns in both the E-plane and H-plane.

The reflection coefficient ($|S_{11}|$) is a key parameter in assessing the resonance behaviour and impedance matching of the sensor. The measured and simulated $|S_{11}|$ for the scenario without AMC are compared in Fig. 34(a). The measured results closely match the simulated results, with a slight deviation due to fabrication tolerances and experimental setup imperfections. The reflection coefficient exhibits a broader resonance, indicating a less focused response. When AMC is integrated, the $|S_{11}|$ curve becomes sharper and more pronounced, as shown in Fig. 34(b). The measured results validate the simulated behaviour, demonstrating improved resonance and better impedance matching. The AMC layer significantly enhances the sensor's performance by reducing unwanted reflections and focusing the energy more effectively.

XXXX-XXXX © XXXX IEEE. Personal use is permitted, but republication/redistribution requires IEEE permission.
See http://www.ieee.org/publications_standards/publications/rights/index.html for more information.
This work is licensed under a Creative Commons Attribution 4.0 License. For more information, see https://creativecommons.org/licenses/by/4.0/

This article has been accepted for publication in IEEE Sensors Journal. This is the author's version which has not been fully edited and
content may change prior to final publication. Citation information: DOI 10.1109/JSEN.2026.3668988

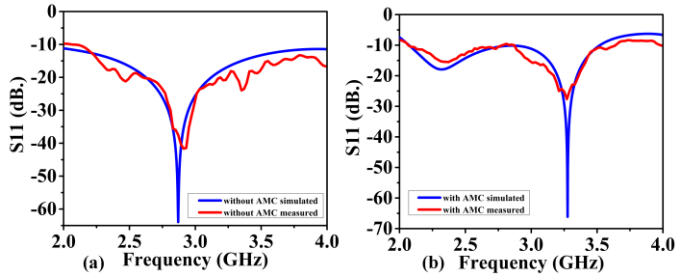

Figure 34: Illustrates the measured and simulated reflection coefficient |S11| for the proposed system, showcasing (a) the scenario without AMC and (b) with AMC.

The realized gain of the sensor was measured and compared with the simulated results to evaluate the impact of AMC on the sensor's performance. Shown in Fig. 35(a), without AMC, the realized gain remains relatively low and stable across the frequency range, with minimal directional enhancement. The measured results show good agreement with the simulated values, confirming the baseline performance of the patch antenna. With AMC integration, the realized gain increases significantly near the resonant frequency, as shown in Fig. 35(b). The measured results closely follow the simulated behaviour, validating the AMC's role in enhancing the sensor's gain. The peak gain improvement demonstrates the AMC's ability to focus electromagnetic energy, which is critical for high-sensitivity and directional sensing applications.

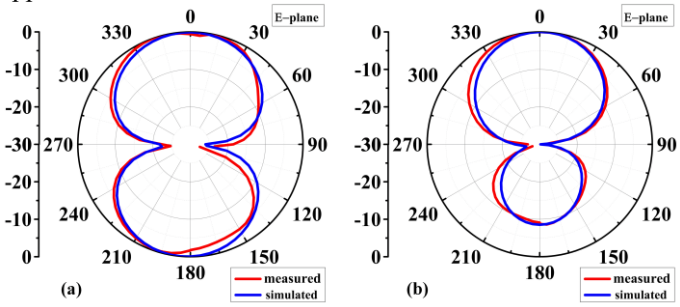

Figure 35: Displays the measured and simulated realized gain of the proposed antenna under two conditions: (a) without AMC and (b) with AMC.

The normalized 2D radiation patterns were measured at the resonant frequency to analyse the sensor's directional characteristics in both the E-plane and H-plane. In Fig. 36(a), the E-plane radiation pattern without AMC exhibits broader side lobes and reduced main lobe sharpness. The measured results align with the simulated patterns, confirming the sensor's baseline radiation behaviour. As shown in Fig. 36(b), with AMC integration, the E-plane pattern shows significant improvement. The side lobes are suppressed, and the main lobe becomes sharper and more focused, indicating enhanced directionality. The measured results closely match the simulated patterns, validating the AMC's contribution to radiation pattern improvement.

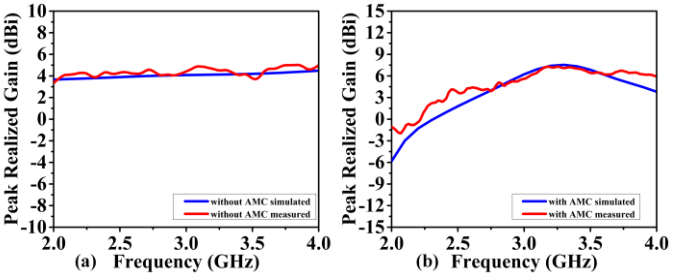

Figure 36: Illustrates the 2D normalized E-plane radiation patterns of the proposed sensor, both simulated and measured at the resonant frequency: (a) represents the pattern without AMC, (b) depicts the pattern with AMC.

The H-plane radiation pattern without AMC reveals significant back radiation and energy dispersion, as shown in Fig. 37(a). The measured results confirm the simulated behaviour, demonstrating the limitations of the baseline design. With AMC, as shown in Fig. 37(b), the H-plane radiation pattern exhibits reduced back radiation and improved beam focus. The main lobe is more pronounced, ensuring efficient energy transmission in the desired direction. The measured and simulated results show strong agreement, further validating the sensor's improved performance.

The experimental validation of the proposed metamaterial-based sensor confirms its high performance in terms of resonance, gain, and directional radiation characteristics. The integration of the AMC layer significantly enhances the sensor's reflection coefficient, realized gain, and radiation patterns, as demonstrated through both simulation and measurement.

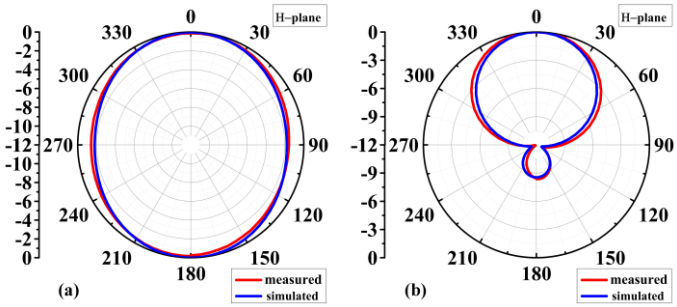

Figure 37: Illustrates the 2D normalized H-plane radiation patterns of the proposed sensor, both simulated and measured at the resonant frequency: (a) displays the pattern without AMC, (b) presents the pattern with AMC.

VI. Distinction Between Antenna Integration And Sensor Capabilities

While the proposed sensor integrates a microstrip patch antenna to facilitate efficient electromagnetic wave excitation and reception, it is important to clearly distinguish between the antenna's supportive role and the core sensing functionality driven by the metamaterial and AMC layers.

The microstrip patch antenna, enhanced by AMC backing, contributes significantly to improving gain, directionality, and radiation efficiency. These enhancements enable effective delivery and collection of electromagnetic signals, which are necessary for reliable sensor operation in GHz-range biomedical applications. However, these improvements primarily influence the signal strength and do not govern the sensor's intrinsic sensing characteristics.

By contrast, the sensing capabilities, such as sensitivity, dielectric contrast resolution, and spectral response shift, are governed by the metamaterial-based structure, specifically its DNG characteristics. The DNG metamaterial exhibits simultaneous negative permittivity and permeability, resulting in a negative refractive index that strengthens field localization and enhances interaction with biological tissues. This field confinement is essential for detecting subtle dielectric variations, such as those associated with tumors or hemorrhagic regions in brain tissue.

XXXX-XXXX © XXXX IEEE. Personal use is permitted, but republication/redistribution requires IEEE permission.
See http://www.ieee.org/publications_standards/publications/rights/index.html for more information.
This work is licensed under a Creative Commons Attribution 4.0 License. For more information, see https://creativecommons.org/licenses/by/4.0/

This article has been accepted for publication in IEEE Sensors Journal. This is the author's version which has not been fully edited and
content may change prior to final publication. Citation information: DOI 10.1109/JSEN.2026.3668988

The integrated AMC layer further amplifies sensing performance by acting as a high-impedance surface. It minimizes backscattering, improves impedance matching, and focuses energy on the sensing region, which collectively enhances the signal-to-noise ratio and overall diagnostic accuracy.

It is important to note that while the antenna optimizes electromagnetic interfacing, it does not alter the sensor's inherent selectivity or dielectric sensitivity. Even when antenna parameters are fixed, the sensor's performance remains robust due to the metamaterial design. This underscores that the core functionality is rooted in the electromagnetic behavior of the DNG and AMC layers.

Additionally, the compact form factor (50 × 50 mm²) and the use of a low-cost FR4 substrate further support the claim that the sensor technology is scalable, cost-effective, and not dependent on complex antenna architectures. This reinforces the sensor's viability as a standalone diagnostic platform, adaptable across a range of biomedical scenarios.

VII. Brain Abnormality Detection

Microwave imaging (MWI) has emerged as a promising non-invasive technique for identifying brain abnormalities by exploiting the dielectric contrast between healthy and pathological tissues. In this study, a unified MWI system equipped with four high-gain sensors (Fig. 38(b), Fig. 42(b)) was employed to investigate two significant neurological conditions: brain tumors and stroke. A seven-layer anatomical brain model (Figs. 38(a), 42(a)), whose electromagnetic properties are summarized in Table 3, was used to simulate realistic human head conditions. The proposed sensor demonstrated double-negative advantages, simultaneously addressing cancerous growth and vascular injury, offering high diagnostic versatility across a broad frequency band of 2 GHz to 4 GHz. This specifically selected operational range of 2 GHz to 4 GHz represents an optimal window that uniquely balances penetration depth and spatial resolution, enabling effective imaging of deep-seated brain tissues. Frequencies below this range typically suffer from insufficient resolution, while those above it tend to experience reduced penetration and elevated signal attenuation, resulting in image degradation due to noise. Therefore, this range not only offers a wide operational bandwidth but also stands out for its exceptional ability to maintain imaging clarity and depth sensitivity simultaneously, crucial for accurately detecting abnormalities located in the deeper regions of the brain.

TABLE 3: Electrical Properties of Different Tissues in the Hemispheric Head Model *[40, 55, 56]*.

Tissue	Electrical or Effective Conductivity (σ_{eff}) (S.m^{-1})	Relative Permittivity (ε_r)
Brain	1.29	43.22
Cerebrospinal fluid (CSF)	2.3	70.1
Dura	0.9	46
Bone (Skull)	0.03	5.6
Fat	0.04	5.54
Skin	0.73	45
Tumor	7	55
Hemorrhagic Stroke	1.58	61.07
Ischemic Stroke	0.85	34

A. Brain Cancer Detection

Brain tumors are typically associated with increased cellular heterogeneity and abnormal proliferation, which result in noticeable variations in dielectric properties when compared to healthy brain tissue. The microwave imaging system exploits these differences to accurately localize and characterize tumor regions. The experimental validation was carried out across three key scenarios: a tumor-free brain phantom, an early-stage tumor model with a 4 mm lesion, and a more aggressive model containing multiple tumors. In the latter case, the secondary tumor was located 18 mm from the first and had a radius of 4.2 mm. The presence of tumor cells significantly increased the localized electric field intensity, thereby enhancing imaging contrast and enabling precise detection, as illustrated in Fig. 39.

The detection efficacy was further examined across four distinct early-stage brain tumor cases. Fig. 40(a) depicts a healthy brain, while Figs. 40(b) and 40(c) illustrate tumors with radii of 3 mm and 4 mm, respectively. Similarly, Fig. 41(a) presents another healthy brain model, while Figs. 41(b) and 41(c) reveal tumors of 5 mm and 6 mm radius, respectively. These findings underscore the sensor's capacity to detect and distinguish tumors of varying sizes, which is essential for staging and treatment planning. Early identification is critical in improving patient outcomes, as it increases the likelihood of complete surgical resection and minimizes the risk of damage to surrounding neural structures. Additionally, early intervention reduces the chance of metastasis, thereby improving long-term survival.

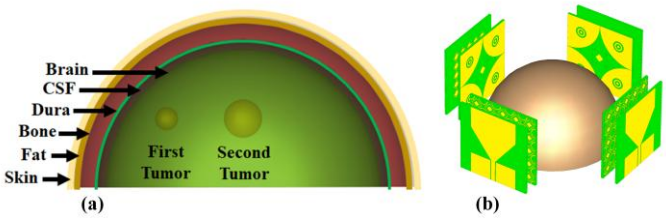

Figure 38: Simulation-based utilization of the proposed sensing system for brain cancer diagnosis: (a) model of a brain phantom containing a tumor; (b) electromagnetic simulation configuration for microwave imaging implementation.

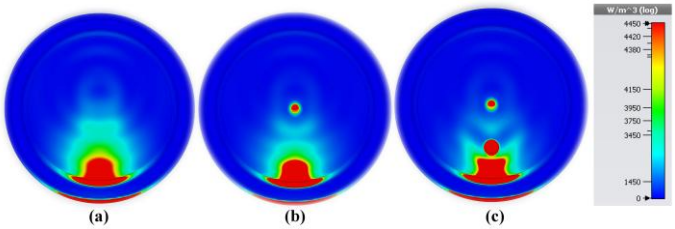

Figure 39: Visualization of microwave imaging output based on electric and magnetic field power loss density at 3.276 GHz: (a) brain model without abnormalities; (b) scenario with an early-stage tumor; and (c) case including two distinct tumor regions.

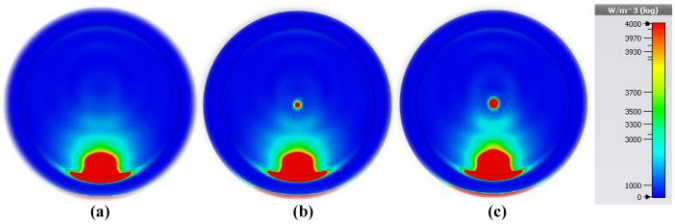

XXXX-XXXX © XXXX IEEE. Personal use is permitted, but republication/redistribution requires IEEE permission.
See http://www.ieee.org/publications_standards/publications/rights/index.html for more information.
This work is licensed under a Creative Commons Attribution 4.0 License. For more information, see https://creativecommons.org/licenses/by/4.0/

This article has been accepted for publication in IEEE Sensors Journal. This is the author's version which has not been fully edited and
content may change prior to final publication. Citation information: DOI 10.1109/JSEN.2026.3668988

Figure 40: Characterization of tumor progression through power loss density mapping at 3.276 GHz using E-field and H-field data: (a) control (healthy brain); (b) first tumor case; (c) second tumor case.

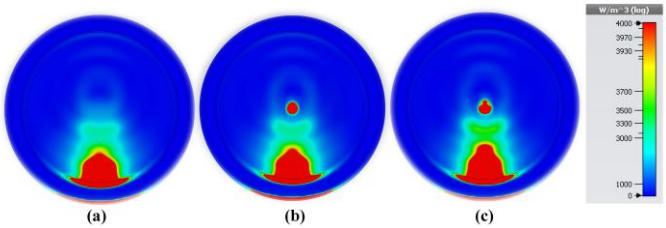

Figure 41: Comparative analysis of tumor volumetric alterations via microwave power loss distribution at 3.276 GHz: (a) reference brain model; (b) third tumor condition; and (c) fourth tumor scenario.

B. Stroke Detection

The proposed sensor also exhibits robust performance in detecting cerebrovascular accidents, commonly referred to as strokes, which can be categorized into ischemic (blockage) and hemorrhagic (bleeding) types. Both stroke types result in distinguishable dielectric shifts due to changes in tissue composition, making MWI particularly suitable for their diagnosis. The selected frequency band (2–4 GHz) supports comprehensive penetration and resolution, enabling the detection of lesions at various depths.

For hemorrhagic stroke, four test scenarios were investigated. A healthy brain model is shown in Fig. 43(a), while hemorrhages with radii of 4 mm, 5 mm, 6 mm, and 7 mm are presented in Figs. 43(b), 43(c), 44(b), and 44(c), respectively. Similarly, ischemic stroke cases were evaluated using four phantoms. Healthy brain references are shown in Figs. 45(a) and 46(a). Corresponding ischemic regions of increasing severity, 4 mm, 5 mm, 6 mm, and 7 mm, are shown in Figs. 45(b), 45(c), 46(b), and 46(c), respectively. The MWI system consistently detected changes in field strength correlated with the presence and severity of both stroke types, enabling effective localization and sizing.

The sensor's performance was benchmarked against state-of-the-art designs detailed in Table 4. The comparative analysis considered sensor size, substrate material, operational frequency, and field characteristics such as realized gain. Our sensor demonstrated a significantly wider bandwidth and superior gain, which are pivotal for high-resolution imaging. Furthermore, the highly directive radiation pattern of the antenna enhances sensitivity and accuracy, surpassing most existing solutions, which are typically optimized for either tumor or stroke detection alone. In contrast, our proposed system offers dual-pathology detection within a single configuration, enhancing its clinical applicability and cost-effectiveness.

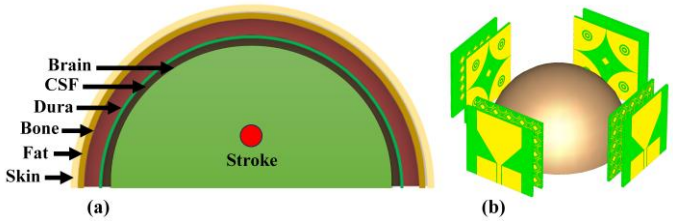

Figure 42: Implementation of the proposed sensor architecture in stroke diagnosis applications: (a) digital representation of a brain phantom with hemorrhagic stroke; (b) computational setup for the microwave imaging process.

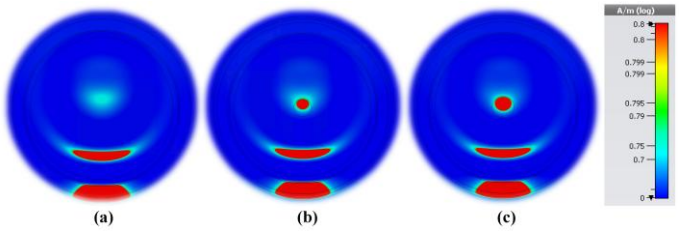

Figure 43: Detection of hemorrhagic stroke volume variations using simulated H-field power loss density at 3.276 GHz: (a) normal brain reference; (b) first hemorrhage condition; and (c) second hemorrhage condition.

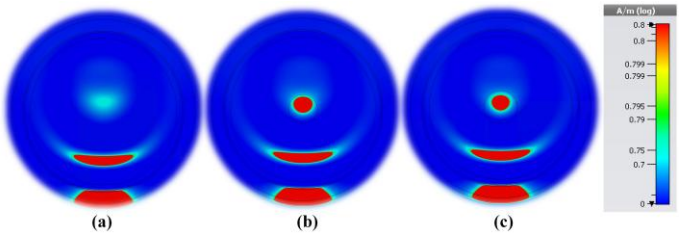

Figure 44: Further assessment of hemorrhagic lesion evolution through H-field imaging at 3.276 GHz: (a) healthy brain reference; (b) third hemorrhagic instance; (c) fourth hemorrhagic instance.

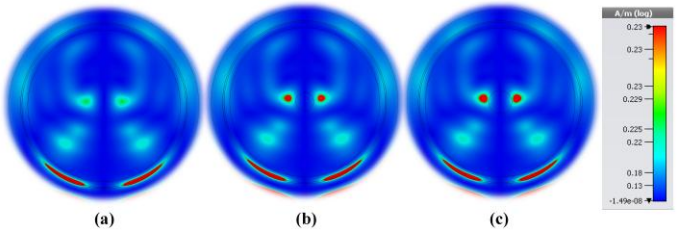

Figure 45: Investigation of ischemic stroke characteristics through H-field power loss imaging at 3.276 GHz: (a) normal brain reference; (b) first ischemic model; (c) second ischemic model.

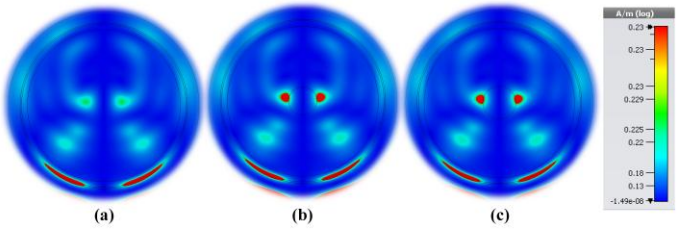

Figure 46: Continued evaluation of ischemic stroke effects using H-field-based imaging at 3.276 GHz: (a) healthy brain model; (b) third ischemic scenario; (c) fourth ischemic scenario.

VIII. Safety and Biocompatibility Considerations

The proposed metamaterial-based biomedical sensor is designed for non-invasive use in the 2–4 GHz frequency range, ensuring safe operation and compliance with international electromagnetic exposure standards. During experimental testing, a 2 mm Teflon spacer was placed between the sensor and the test sample to maintain a controlled separation and to reduce direct electromagnetic coupling with biological tissue. Teflon ($\varepsilon_r \approx 2.1$, $\tan\delta \approx 0.0002$) is a widely accepted biocompatible, low-loss dielectric that preserves field uniformity while providing a safe operational buffer.

Regarding exposure safety, the sensor operates at power levels well below the limits defined by IEEE C95.1-2019 and ICNIRP 2020 for localized Specific Absorption Rate (SAR).

XXXX-XXXX © XXXX IEEE. Personal use is permitted, but republication/redistribution requires IEEE permission.
See http://www.ieee.org/publications_standards/publications/rights/index.html for more information.
This work is licensed under a Creative Commons Attribution 4.0 License. For more information, see https://creativecommons.org/licenses/by/4.0/

This article has been accepted for publication in IEEE Sensors Journal. This is the author's version which has not been fully edited and content may change prior to final publication. Citation information: DOI 10.1109/JSEN.2026.3668988

These guidelines specify maximum localized SAR values of 2 W/kg averaged over 10 g of tissue for the head and torso, and 4 W/kg for limbs within the 2–4 GHz range. Based on simulated field intensities and the measured input power used in this work (≤ 10 dBm), the expected SAR values remain far below these regulatory thresholds. Additionally, the AMC backing and DNG metamaterial layer improve forward radiation while suppressing backward emissions, further reducing unnecessary electromagnetic exposure to nearby tissue.

The sensor's configuration supports safe, non-invasive operation for on-body or near-head biomedical diagnostics. Future work will include full-wave SAR analysis using anatomically realistic tissue phantoms to quantify spatial power absorption and verify compliance under wearable and clinical conditions.

IX. Benchmarking

A comparative analysis of the proposed sensor with recently published biomedical sensors operating in the microwave frequency range is provided in Table 4. Key metrics, including structure size, substrate type, operational frequency range, and peak gain, are used to benchmark performance.

The proposed sensor demonstrates multiple novel advantages over existing solutions:

1. *Compact and Efficient Form Factor*: With a structure size of 50 × 50 mm², the sensor offers a balanced design that is more compact than many prior works (e.g., [43], [57], [58], and [59]) while still maintaining high radiation efficiency and structural simplicity. This compactness is critical for wearable and portable biomedical systems.
2. *High Gain on Cost-Effective Substrate*: Despite being fabricated on standard FR4 substrate, commonly considered lossy compared to premium materials like Rogers RO4350B or RT5880, the sensor achieves a peak gain of 7.6 dBi, which is superior to all referenced works in Table 4, including those using high-end substrates. For instance, [40] achieves 5.65 dBi and [59] 5.19 dBi. This highlights the effectiveness of the AMC + DNG metamaterial integration strategy.
3. *Broadband GHz Compatibility*: The sensor operates across the 2–4 GHz band, making it suitable for a wide range of biomedical diagnostic applications. In contrast, many existing designs are limited to narrower sub-bands ([36], [42]) or lower frequencies ([58], [60]).
4. *Superior Sensitivity and FoM*: Table 5 provides a direct performance comparison against recent metamaterial-based biomedical sensors. The proposed design shows significantly higher sensitivity (0.4527 GHz RIU^{-1}), Q-factor (175.18), and Figure of Merit (24.21 RIU^{-1}), all of which are essential for detecting subtle dielectric variations in biological tissues.
5. *Unique Structural Integration*: Most notably, the sensor uniquely integrates a double-negative (DNG) metamaterial with an AMC-backed microstrip patch antenna, a configuration not found in any of the compared designs. While some works employ AMC alone or SRR-based MTMs, none combine both AMC and DNG metamaterials within a dual-band architecture optimized for biomedical sensing. This integration achieves both high sensitivity and directional precision without increasing complexity or cost.

The proposed sensor sets a new benchmark among GHz-range biomedical sensors by delivering:

- Best-in-class gain on FR4 substrate
- High sensitivity and narrowband performance in a broadband system
- Compact size suitable for real-world biomedical integration
- A novel AMC+DNG architecture not explored in prior literature

These attributes collectively distinguish this work in terms of both technical innovation and practical applicability, making it a strong candidate for next-generation portable biomedical diagnostic platforms.

TABLE 4: Performance Comparison Between the Proposed Sensor and Advanced Biomedical Sensors Operating Within the 1 GHz to 4 GHz Frequency Range.

Ref.	Structure Size (mm^2)	Substrate	Frequency Range (GHz)	Gain (dBi)	Year Published
[57]	70×30	GIL 1023	1.1–3.4	< 4	2014
[61]	80×20	FR4	1.1-2.2	3.15	2016
[62]	70 × 15	Rogers 3003	0-3.5	3	2016
[62]	70×15	Rogers RT3000	1.1-3.2	3	2016
[60]	29.99×29.99	FR4	0.902-0.928	< 3	2018
[58]	59×59	Rogers R04003C	0.6-1.4	3.1	2019
[63]	50 × 60	Rogers RO4350B	2-3	2.45	2019
[31]	50×44	Rogers RO4350B	0.55-3	< 4	2020
[40]	50 × 44	Rogers RO4350B	1.5–4	5.65	2020
[64]	50×70	FR4	1-2	-	2020
[43]	70×30	Rogers RT5880	2.2-4	5	2022
[36]	33.2 × 46.8	PTFE	2.7-2.8	6	2023
[42]	40×40	FR4	2.8-2.85	7.6	2023
[65]	46×30	FR4	1.5-4.5	3.14	2023
[44]	20×20	RT5880	3.5-13	5.6	2024
[59]	50 × 60	RT5880	2.1, 4.1	2.2, 5.19	2025
This work	50 × 50	FR4	2–4	7.6	-

The sensitivity of a microwave or GHz-range metamaterial-based sensor is a key indicator of its ability to detect small variations in the dielectric constant or refractive index of the surrounding medium. In this study, sensitivity is quantified by measuring the shift in the sensor's resonance frequency resulting from changes in the effective permittivity of the material under test.

Three primary parameters define the overall performance of a resonant sensor: Sensitivity (S), Quality Factor (Q), and Figure of Merit (FOM). Each metric highlights a different aspect of sensing behavior and together provides a

XXXX-XXXX © XXXX IEEE. Personal use is permitted, but republication/redistribution requires IEEE permission.
See http://www.ieee.org/publications_standards/publications/rights/index.html for more information.
This work is licensed under a Creative Commons Attribution 4.0 License. For more information, see https://creativecommons.org/licenses/by/4.0/

This article has been accepted for publication in IEEE Sensors Journal. This is the author's version which has not been fully edited and content may change prior to final publication. Citation information: DOI 10.1109/JSEN.2026.3668988

comprehensive assessment of detection accuracy and efficiency.

The Figure of Merit (FOM), which represents the sensor's selectivity and resolution, is defined as the ratio between the sensitivity and the full width at half maximum (FWHM) of the resonance response:

$$FOM = \frac{S}{FWHM} \tag{6}$$

Higher FOM indicates stronger discrimination between neighboring resonance frequencies, implying higher precision in dielectric detection.

The Quality Factor (Q-factor) measures the sharpness of the resonance, defined as:

$$Q_{factor} = \frac{\lambda}{FWHM} \tag{7}$$

where λ is the resonant wavelength. A higher Q-factor reflects a narrower resonance dip, indicating improved sensitivity to small perturbations in the dielectric environment.

The sensitivity (S) itself can be defined in two main ways in scientific literature. For frequency-based microwave biosensors, the frequency sensitivity is given as:

$$S = \frac{\Delta f}{\Delta n} \tag{8}$$

where Δf denotes the change in the resonance frequency and Δn is the variation in the refractive index (RI) of the analyte, measured in refractive index units (RIU). This metric, expressed in GHz/RIU, quantifies how much the resonant frequency shifts per unit change in refractive index.

Alternatively, for intensity-based sensing, the intensity sensitivity may be defined as:

$$S = \Delta I / \Delta n \tag{9}$$

where ΔI represents the change in the resonant intensity corresponding to the refractive index variation. However, since the proposed sensor primarily operates based on resonance frequency shift rather than intensity modulation, the frequency sensitivity (Equation 8) is adopted as the governing metric.

For the proposed AMC–DNG metamaterial-based sensor, dielectric loading simulations were performed by varying the effective refractive index (n) of the material placed above the structure. The resulting resonance frequency shift (Δf) demonstrated a linear dependence on Δn, confirming a stable and predictable sensing response throughout the 2–4 GHz operating band. From this linear relationship, the average frequency sensitivity was calculated as 0.4527 GHz/RIU. The corresponding Q-factor and FOM were determined to be 175.18 and 24.21 RIU^{-1}, respectively, indicating strong spectral selectivity and high precision in detecting dielectric variations.

These quantitative results verify the sensor's suitability for GHz-range biomedical diagnostics, where reliably distinguishing subtle dielectric differences, such as those between healthy and malignant tissues, is essential.

Based on the comparative data presented in Table 5, the proposed biosensor demonstrates a significant leap in performance over existing designs for biomedical applications. The sensor's Figure of Merit (FoM) of 24.21 RIU^{-1} is the highest among all compared sensors, more than double the next highest value of 12 from reference [66]. This metric, which encapsulates both sensitivity and spectral sharpness, underscores the sensor's superior overall effectiveness. While the sensitivity of 0.4527 GHz RIU^{-1} is also a leading value in the S-band, its exceptional performance is primarily driven by its Quality Factor (Q-factor) of 175.18, which is the highest in the benchmark, indicating an extremely sharp and well-defined resonance peak. This high Q-factor ensures high precision and robust detection capabilities, crucial for distinguishing subtle dielectric variations in biological tissues.

The novelty of this work is established through the synergistic combination of double-negative metamaterial characteristics and an Artificial Magnetic Conductor (AMC) layer. This innovative design approach has enabled the sensor to achieve an optimal balance between sensitivity and selectivity that surpasses the performance of previously published works. For instance, sensors from references [67] and [66], while also operating in the S-band with commendable sensitivity, lack the high Q-factor and FoM of the proposed design. The sensor from reference [68], a microwave filter, exhibits a high Q-factor of 160 but is not optimized for the specific requirements of biomedical sensing, such as detecting minute changes in the dielectric properties of biological samples. The proposed sensor's superior performance, as validated by these benchmarks, establishes it as a highly promising candidate for advanced medical imaging, wearable health monitoring, and non-invasive diagnostics.

Crucially, among all compared designs, ours is the only sensor that integrates both AMC and DNG metamaterial structures, enabling dual-band operation and high directionality without compromising cost or size. This unique architectural combination contributes directly to the enhanced performance metrics, setting our work apart from existing solutions and reinforcing its suitability for GHz-range biomedical diagnostics such as brain imaging and wearable health monitoring.

TABLE 5: COMPARATIVE PERFORMANCE ANALYSIS OF METAMATERIAL-BASED BIOMEDICAL SENSORS.

Refs.	Figure of merit (FoM)	Operating band (GHz)	Sensitivity	Quality factor	Application
[68]	6.33	S-band	20–100 mg/mL	160	Microwave filter
[69]	1.7	C-band	0.04	46	Material sensor
[70]	7.3	C-band	− 3dB/mm	120	Thickness sensor
[67]	11.05 RIU^{-1}	S-band	0.3537 GHz RIU^{-1}	110	Permittivity sensor
[71]	2	C-band	0.03	75	Liquid sensor
[72]	1	S-band	0.1	35	Material sensor
[73]	1	L-band	0.13	60	Liquid sensor
[66]	12	S-band	0.46	44	Liquid sensor
This work	24.21 RIU^{-1}	S-band	0.4527 GHz RIU^{-1}	175.18	Biomedical sensor

X. COMPARATIVE ANALYSIS AND NOVELTY

To assess the advancement offered by the proposed compact and low-cost AMC-backed double-negative (DNG) metamaterial sensor, a comprehensive benchmarking study

XXXX-XXXX © XXXX IEEE. Personal use is permitted, but republication/redistribution requires IEEE permission.
See http://www.ieee.org/publications_standards/publications/rights/index.html for more information.
This work is licensed under a Creative Commons Attribution 4.0 License. For more information, see https://creativecommons.org/licenses/by/4.0/

This article has been accepted for publication in IEEE Sensors Journal. This is the author's version which has not been fully edited and
content may change prior to final publication. Citation information: DOI 10.1109/JSEN.2026.3668988

was conducted against recent GHz-range biomedical and wearable antenna designs published from 2023 to 2025. These comparative works, summarized in Table 6, were selected based on their use of metamaterial or AMC structures to enhance sensitivity, gain, or dielectric characterization performance.

The proposed design exhibits three key innovations that collectively advance the state of the art. First, it achieves an experimentally verified realized gain of 7.6 dBi on a standard FR4 substrate, surpassing most contemporary sensors despite the substrate's known dielectric losses. Second, it demonstrates simultaneous negative permittivity (ε) and permeability (μ), yielding a negative refractive index across the 2.0–2.7 GHz band. This property strengthens electromagnetic field confinement and significantly improves sensing precision. Third, the integration of an AMC layer creates an electromagnetic lensing effect that enhances forward radiation, directionality, and dielectric sensitivity.

The resulting sensing performance, characterized by a sensitivity of 0.4527 GHz·RIU^{-1}, a quality factor of 175.18, and a FOM of 24.21 RIU^{-1}, ranks among the highest reported for GHz-range metamaterial-based biomedical sensors. This synergistic AMC–DNG–patch architecture provides a unique combination of high sensitivity, compact design, and straightforward manufacturability, underscoring its promise for practical deployment in portable biomedical imaging and diagnostic systems.

XI. Future perspective

Future investigations will focus on evaluating the sensor's performance in realistic biomedical environments. This includes conducting in vitro and in vivo studies to assess its ability to detect specific biomarkers or image biological tissues in complex media. The development of robust signal processing algorithms will be crucial for extracting meaningful information from the sensor's output in the presence of noise and interference. Ultimately, the goal is to translate this technology into clinical applications, requiring rigorous testing and validation to ensure its safety and efficacy for diagnostic and therapeutic purposes.

XII. Conclusions

In this work, a novel metamaterial-based biomedical sensor was proposed, designed, and experimentally validated for operation within the 2–4 GHz frequency range. The key innovation lies in the unique integration of a double-negative (DNG) metamaterial structure with an artificial magnetic conductor (AMC)-backed microstrip patch antenna, a configuration not reported in previous GHz-range biomedical sensors. This hybrid architecture enables simultaneous enhancement of directionality, gain, and sensitivity, while maintaining a compact footprint of 50 × 50 mm² on a cost-effective FR4 substrate.

The sensor achieves a peak gain of 7.6 dBi, surpassing all other comparable sensors reported in the literature operating within the same frequency range, including those using high-end substrates. Its dual-band behavior and strong dielectric sensitivity are further supported by both simulation and experimental measurements conducted in a controlled anechoic environment. The results for reflection coefficient, realized gain, and radiation patterns show excellent agreement between simulation and measurement, validating the design's effectiveness.

A comprehensive benchmarking analysis clearly demonstrates the superior performance of the proposed sensor in terms of gain, sensitivity, Q-factor, and Figure of Merit (FoM). Notably, it is the only design to combine AMC and DNG metamaterial structures within a low-cost, compact, and broadband system tailored for biomedical diagnostics. These advantages make the sensor particularly suited for precision diagnostics, wearable health monitoring systems, and GHz-range medical imaging.

Looking ahead, future research will explore further miniaturization, bandwidth enhancement, and real-world clinical testing. Additionally, efforts will be made to integrate the sensor with flexible and biocompatible substrates to enable next-generation wearable and implantable biomedical platforms.

XIII. Practical Constraints and Future Research Directions

Although the proposed double-negative (DNG) metamaterial sensor integrated with an AMC-backed antenna demonstrates strong experimental performance and clear potential for GHz-range biomedical diagnostics, several practical considerations must be addressed before clinical translation. The present work focuses primarily on electromagnetic characterization under controlled free-space conditions using standard dielectric substrates. While these results confirm the sensor's high gain, sensitivity, and directionality, they do not fully capture the effects of tissue heterogeneity, lossy biological media, or safety requirements such as specific absorption rate (SAR) compliance.

An essential next step is the experimental validation of dielectric-contrast sensitivity using tissue-equivalent phantoms or biogel samples that replicate the electromagnetic properties of human tissues in the 2–4 GHz range. Such measurements will enable quantitative assessment of the sensor's ability to detect pathological variations—including early-stage brain abnormalities and soft-tissue anomalies—and will provide insight into signal attenuation, penetration depth, and reflection behavior in realistic biomedical environments. Phantom-based testing will therefore serve as a critical bridge between simulation-driven benchmarking and practical diagnostic applicability.

Future work will also explore the development of biocompatible and flexible sensor variants using substrates such as PDMS or polyimide to support wearable deployment. Additional research will focus on SAR reduction strategies, adaptive impedance tuning for real-time sensing, and the use of numerical head and body models to analyze near-field coupling and power absorption in biological tissues.

Collectively, these research directions will strengthen the biomedical relevance of the proposed AMC–DNG architecture by addressing its current experimental limitations and establishing a clear pathway toward safe, ethical, and clinically validated GHz-range diagnostic systems.

XXXX-XXXX © XXXX IEEE. Personal use is permitted, but republication/redistribution requires IEEE permission.
See http://www.ieee.org/publications_standards/publications/rights/index.html for more information.
This work is licensed under a Creative Commons Attribution 4.0 License. For more information, see https://creativecommons.org/licenses/by/4.0/

This article has been accepted for publication in IEEE Sensors Journal. This is the author's version which has not been fully edited and content may change prior to final publication. Citation information: DOI 10.1109/JSEN.2026.3668988

Involvement of Human Participants
No human participants were included in this study.

Declaration of Competing Interests
The authors have no competing interests to declare.

Availability of Data
The datasets utilized or analyzed during the present study are available from the corresponding author upon reasonable request.

TABLE 6: COMPARATIVE BENCHMARKING OF THE PROPOSED AMC-BACKED DOUBLE-NEGATIVE (DNG) METAMATERIAL SENSOR WITH RECENT GHZ-RANGE BIOMEDICAL AND WEARABLE ANTENNA DESIGNS (2023–2025).

Ref (first author, year)	Application / Note	Freq (GHz)	Substrate	Footprint (mm²)	Peak gain (dBi)	Sensitivity / Q / FoM (as reported)	Key design note
Yadav et al., 2023. Intl. J. Microwave & Wireless Tech. [74]	Wearable AMC-backed monopole (biomedical/ wearable)	5.8 GHz	RO3003	36 ×36	7.5	–	6×6 AMC array backing; wearable target; gain improvement with AMC
Jagadeesan et al., 2023. Appl. Phys. A[75]	Metamaterial sensor antenna for breast-cancer	2.35–2.52 GHz	FR-4 (or stated substrate)	reported small patch size	~2.4 dB	Resonances shift with tissue permittivity; sensitivity reported (resonance shift)	SRR + Minkowski DGS; tested with cancer cell lines
Datta et al., 2023. (metamaterial lens + MWI) [76]	Metamaterial lens for microwave imaging	2–4 GHz band (imaging)	FR-4	150 ×150	—	—	Demonstrates metamaterial lens improving MWI resolution
Wongkasem et al., 2024. PMC (multiple-point MTM sensors) [77]	Multiple-point metamaterial microwave sensors	14.8–15 GHz reported	Various (substrates)	compact	low-to-moderate gains reported	Sensitivity values reported for multiple points	MTM-inspired multi-band sensors for microwave sensing
Chowdhury et al., 2025. Sci. Rep. [78]	Flexible MTM microwave sensor (6.72 GHz, 8.65 GHz resonances)	6.72 GHz, 8.65 GHz	Rogers RT-5880 or flexible substrate	small cell size	—	Sensitivity 0.033 GHz $\Delta\varepsilon^{-1}$; Q = 80.39; FoM = 26.52 $\Delta\varepsilon^{-1}$	Flexible metamaterial resonator; high EMR; dual-side sensing
Multiple recent MTM biomedical works (2023–2024 review) [79]	Reviews and comparative studies	various	various	—	—	Summary metrics provided	Reviews summarize trends and report comparable metrics
This work (proposed)	AMC + Double-Negative metamaterial sensor for biomedical MWI & wearable use	2.0–4.0 GHz (selected band)	FR4 (1.52 mm)	50 × 50 mm²	7.6 dBi (measured)	Sensitivity 0.4527 GHz RIU^{-1}; Q = 175.18; FoM = 24.21 RIU^{-1} (Table 5)	Unique concurrent integration of DNG metamaterial + AMC + patch antenna on low-cost FR4; experimental validation in anechoic chamber

REFERENCES

[1] Q. Zhao, J. Zhou, F. Zhang, and D. Lippens, "Mie resonance-based dielectric metamaterials," *Materials today,* vol. 12, no. 12, pp. 60-69, 2009.

[2] F. Bendelala, A. Cheknane, and H. S. Hilal, "A broad-band polarization-insensitive absorber with a wide angle range metamaterial for thermo-photovoltaic conversion," *Optical and Quantum Electronics,* vol. 50, pp. 1-10, 2018.

[3] S. Jiang, Q. Zong, and X. Deng, "Application analysis of GPS positioning technology and GIS based on metamaterial in forestry engineering," in *E3S Web of Conferences*, 2019, vol. 118, p. 03059: EDP Sciences.

[4] P. Garg and P. Jain, "Isolation improvement of MIMO antenna using a novel flower shaped metamaterial absorber at 5.5 GHz WiMAX band," *IEEE Transactions on Circuits and Systems II: Express Briefs,* vol. 67, no. 4, pp. 675-679, 2019.

[5] Y. Fan *et al.*, "Recent developments of metamaterials/metasurfaces for RCS reduction," *EPJ Applied Metamaterials,* vol. 6, p. 15, 2019.

[6] H. Chen, W. Ma, Z. Huang, Y. Zhang, Y. Huang, and Y. Chen, "Graphene-based materials toward microwave and terahertz absorbing stealth technologies," *Advanced Optical Materials,* vol. 7, no. 8, p. 1801318, 2019.

[7] K. Shi, G. Jin, R. Liu, T. Ye, and Y. Xue, "Underwater sound absorption performance of acoustic metamaterials with multilayered locally resonant scatterers," *Results in Physics,* vol. 12, pp. 132-142, 2019.

[8] A. Xomalis *et al.*, "Cryptography in coherent optical information networks using dissipative metamaterial gates," *APL Photonics,* vol. 4, no. 4, 2019.

[9] K. Du, Q. Li, W. Zhang, Y. Yang, and M. Qiu, "Wavelength and thermal distribution selectable microbolometers based on metamaterial absorbers," *IEEE Photonics Journal,* vol. 7, no. 3, pp. 1-8, 2015.

[10] C. Wu and M. Soleimani, "Frequency difference EIT with localization: a potential medical imaging tool during cancer treatment," *IEEE Access,* vol. 7, pp. 21870-21878, 2019.

[11] H. N. Patel, "Microwave imaging for breast cancer detection using 3D level set based optimization, FDTD method and method of moments," Dhirubhai Ambani Institute of Information and Communication Technology, 2019.

[12] A. S. Dhillon, D. Mittal, and R. Bargota, "Triple band ultrathin polarization insensitive metamaterial absorber for defense, explosive detection and airborne radar applications," *Microwave and optical technology letters,* vol. 61, no. 1, pp. 89-95, 2019.

[13] A. Rasoulzadeh, C. Ghobadi, and J. Nourinia, "A compact differential microwave fluid sensor for permittivity measurement of ethanol-water solution," *IEEE Sensors Journal,* 2025.

[14] H. Xiong, Y.-J. Liu, J. Deng, Q. Yang, D. Xiao, and B.-X. Wang, "Design of a Broadband Microwave Power Detector Based on Metasurfaces With Linear Response and Thermal Sensing," *IEEE Sensors Journal,* 2025.

[15] M. N. Hamza, S. Koziel, and A. Pietrenko-Dabrowska, "Design and experimental validation of a metamaterial-based sensor for microwave imaging in breast, lung, and brain cancer detection," *Scientific Reports,* vol. 14, no. 1, p. 16177, 2024.

[16] Y. Liu *et al.*, "Multi-peak narrow-band metamaterial absorber for visible to near-infrared wavelengths," *Results in Physics,* vol. 47, p. 106374, 2023.

[17] M. Y. Azab, M. F. O. Hameed, A. M. Nasr, and S. Obayya, "Highly sensitive metamaterial biosensor for cancer early detection," *IEEE Sensors Journal,* vol. 21, no. 6, pp. 7748-7755, 2021.

[18] M. Y. Azab, M. F. O. Hameed, and S. S. Obayya, "Overview of optical biosensors for early cancer detection: fundamentals, applications and future perspectives," *Biology,* vol. 12, no. 2, p. 232, 2023.

[19] A. N. Razani, P. Rezaei, P. Zamzam, S. A. Khatami, and O. M. Daraei, "Absorption-based ultra-sensitive RI sensor based on the flower-shaped graphene resonator for early detection of cancer," *Optics Communications,* vol. 524, p. 128775, 2022.

[20] Z. Qu *et al.*, "Microstructure-based high-quality factor terahertz metamaterial bio-detection sensor," *Advanced Composites and Hybrid Materials,* vol. 6, no. 3, p. 100, 2023.

[21] V. Veselago, "The electrodynamics of substances with simultaneously negative values of and," *Usp. fiz. nauk,* vol. 92, no. 3, pp. 517-526, 1967.

[22] J. B. O. de Araújo, G. L. Siqueira, E. Kemptner, M. Weber, C. Junqueira, and M. M. Mosso, "An ultrathin and ultrawideband metamaterial absorber and an equivalent-circuit parameter retrieval method," *IEEE Transactions on Antennas and Propagation,* vol. 68, no. 5, pp. 3739-3746, 2020.

[23] M. Amiri, F. Tofigh, N. Shariati, J. Lipman, and M. Abolhasan, "Review on metamaterial perfect absorbers and their applications to IoT," *IEEE Internet of Things Journal,* vol. 8, no. 6, pp. 4105-4131, 2020.

[24] D. K. Choudhary and R. K. Chaudhary, "A compact triple band metamaterial inspired bandpass filter using inverted S-shape resonator," *Radioengineering,* vol. 27, no. 2, p. 373, 2018.

[25] N. Bai, W. Xiang, J. Shen, C. Shen, and X. Sun, "A $ Ka $-band folded waveguide traveling wave tube with lumped resistance metamaterial absorber," *IEEE Transactions on Electron Devices,* vol. 67, no. 3, pp. 1248-1253, 2020.

[26] M. N. Hamza, M. T. Islam, and S. Koziel, "Advanced sensor for non-invasive breast cancer and brain cancer diagnosis using antenna array with metamaterial-based AMC," *Engineering Science and Technology, an International Journal,* vol. 56, p. 101779, 2024.

[27] T. Alam, M. Samsuzzaman, M. Faruque, and M. Islam, "A metamaterial unit cell inspired antenna for mobile wireless applications," *Microwave and Optical Technology Letters,* vol. 58, no. 2, pp. 263-267, 2016.

[28] F. Li *et al.*, "Design and implementation of metamaterial polarization converter with the reflection and transmission polarization conversion simultaneously," *Journal of Optics,* vol. 21, no. 4, p. 045102, 2019.

XXXX-XXXX © XXXX IEEE. Personal use is permitted, but republication/redistribution requires IEEE permission.
See http://www.ieee.org/publications_standards/publications/rights/index.html for more information.
This work is licensed under a Creative Commons Attribution 4.0 License. For more information, see https://creativecommons.org/licenses/by/4.0/

This article has been accepted for publication in IEEE Sensors Journal. This is the author's version which has not been fully edited and
content may change prior to final publication. Citation information: DOI 10.1109/JSEN.2026.3668988

[29] M. R. Islam *et al.*, "Quad-band split ring resonator-based sensor for microwave sensing application," *Scientific Reports,* vol. 15, no. 1, p. 6888, 2025.

[30] M. A. Khalil *et al.*, "Double-negative metamaterial square enclosed QSSR for microwave sensing application in S-band with high sensitivity and Q-factor," *Scientific Reports,* vol. 13, no. 1, p. 7373, 2023.

[31] A. S. Alqadami, N. Nguyen-Trong, A. E. Stancombe, K. Bialkowski, and A. Abbosh, "Compact flexible wideband antenna for on-body electromagnetic medical diagnostic systems," *IEEE Transactions on Antennas and Propagation,* vol. 68, no. 12, pp. 8180-8185, 2020.

[32] A. R. Chishti *et al.*, "Advances in antenna-based techniques for detection and monitoring of critical chronic diseases: A comprehensive review," *IEEE Access,* vol. 11, pp. 104463-104484, 2023.

[33] M. A. U. Haq, A. Armghan, K. Aliqab, and M. Alsharari, "A review of contemporary microwave antenna sensors: Designs, fabrication techniques, and potential application," *IEEE Access,* vol. 11, pp. 40064-40074, 2023.

[34] M. Abbak, M. Çayören, and I. Akduman, "Microwave breast phantom measurements with a cavity-backed Vivaldi antenna," *IET Microwaves, Antennas & Propagation,* vol. 8, no. 13, pp. 1127-1133, 2014.

[35] D. O. Rodriguez-Duarte, J. A. T. Vasquez, R. Scapaticci, L. Crocco, and F. Vipiana, "Brick-shaped antenna module for microwave brain imaging systems," *IEEE Antennas and Wireless Propagation Letters,* vol. 19, no. 12, pp. 2057-2061, 2020.

[36] J. George, M. Uko, S. Ekpo, and F. Elias, "Design of an elliptically-slotted patch antenna for multi-purpose wireless Wi-Fi and biosensing applications," *e-Prime-Advances in Electrical Engineering, Electronics and Energy,* vol. 6, p. 100368, 2023.

[37] K. Kaur and A. Kaur, "In vitro detection of skin cancer using an UWB stacked micro strip patch antenna with microwave imaging," *International Journal of RF and Microwave Computer-Aided Engineering,* vol. 32, no. 12, p. e23407, 2022.

[38] W. Lee, S. Oh, and S. K. Hong, "Compact Dual-Circularly Polarized Traveling-Wave Series-Fed Patch Array for Use as a Non-Linear Tag Antenna for Bio-Sensing Applications," *Applied Sciences,* vol. 13, no. 13, p. 7729, 2023.

[39] Y. Mahnashi, K. K. Qureshi, A. A. Al-Shehri, and H. Attia, "Design and experimental validation of a noninvasive glucose monitoring system using RF antenna-based biosensor," *IEEE Sensors Journal,* vol. 23, no. 3, pp. 2856-2864, 2022.

[40] A. Hossain, M. T. Islam, M. E. Chowdhury, and M. Samsuzzaman, "A grounded coplanar waveguide-based slotted inverted delta-shaped wideband antenna for microwave head imaging," *IEEE Access,* vol. 8, pp. 185698-185724, 2020.

[41] S. Saranya, B. Sharmila, P. Jeyakumar, and P. Muthuchidambaranathan, "Design and analysis of metaresonator-based tri-band antenna for biosensing applications," *Plasmonics,* vol. 18, no. 5, pp. 1799-1811, 2023.

[42] N. Dadouche *et al.*, "Design and Fabrication of a Novel Corona-Shaped Metamaterial Biosensor for Cancer Cell Detection," *Micromachines,* vol. 14, no. 11, p. 2114, 2023.

[43] M. S. Islam, M. T. Islam, and A. F. Almutairi, "A portable non-invasive microwave based head imaging system using compact metamaterial loaded 3D unidirectional antenna for stroke detection," *Scientific Reports,* vol. 12, no. 1, p. 8895, 2022.

[44] F.-e. Zerrad, M. Taouzari, E. Almajali, M. Karaaslan, J. El Aoufi, and A. Hussain, "An Improved Breast Cancer Biosensing System Using a Slotted Patch Antenna with a Metamaterial Surface," *IEEE Sensors Journal,* 2024.

[45] S. Patel, A. Singh, D. Mitra, and C. Koley, "Metamaterial-enabled microwave sensor for non-invasive continuous glucose monitoring," *Results in Engineering,* p. 105782, 2025.

[46] S. Douhi, Y. Houssaini, S. Das, V. Subramanian, B. T. P. Madhav, and A. Eddiai, "Metamaterial-integrated wearable UWB antenna with SAR reduction and gain enhancement for Wireless Body Area Sensor Networks (WBASNs): Design and experimental verification," *Sensors and Actuators A: Physical,* vol. 388, p. 116499, 2025.

[47] T. Qiang *et al.*, "Symmetric metamaterial coupling element-based microwave sensor integrated with microfluidic Chip for cell sorting and concentration detection," *Microchemical Journal,* p. 115856, 2025.

[48] R. Maged, A. S. Abd El-Hameed, and E. K. Hamad, "Advances in Wearable Textile Antennas for Biomedical Applications: A Comprehensive Review of Material Variants, Fabrication Techniques, and Design Innovations," *Sensors and Actuators A: Physical,* p. 117132, 2025.

[49] M. Mujahid Hossain and S. Hannan, "Compact Nested Hexagonal Metamaterial Sensor for High-Sensitivity Permittivity Characterization Across S and X-Band Frequencies," *arXiv e-prints,* p. arXiv: 2502.03863, 2025.

[50] M. B. Billa *et al.*, "High quality factor double negative metamaterial for textile fabric and fabric moisture sensing applications," *Journal of Industrial Textiles,* vol. 54, p. 15280837231225828, 2024.

[51] D. C. Tzarouchis, M. Koutsoupidou, I. Sotiriou, K. Dovelos, D. Rompolas, and P. Kosmas, "Electromagnetic metamaterials for biomedical applications: short review and trends," *EPJ Applied Metamaterials,* vol. 11, p. 7, 2024.

[52] Y. Thangavelu, B. Thangaraju, and R. Maheswar, "Design and SAR Analysis of an AMC-Integrated Wearable Cavity-Backed SIW Antenna," *Micromachines,* vol. 15, no. 12, p. 1530, 2024.

[53] A. Nicolson and G. Ross, "Measurement of the intrinsic properties of materials by time-domain techniques," *IEEE Transactions on instrumentation and measurement,* vol. 19, no. 4, pp. 377-382, 2007.

[54] W. B. Weir, "Automatic measurement of complex dielectric constant and permeability at microwave frequencies," *Proceedings of the IEEE,* vol. 62, no. 1, pp. 33-36, 2005.

[55] R. Inum, M. M. Rana, K. N. Shushama, and M. A. Quader, "EBG based microstrip patch antenna for brain tumor detection via scattering parameters in microwave imaging system," *International journal of biomedical imaging,* vol. 2018, 2018.

[56] P. A. Hasgall *et al.*, "IT'IS Database for thermal and electromagnetic parameters of biological tissues," *Version 4.0,* 2018.

[57] A. T. Mobashsher, A. M. Abbosh, and Y. Wang, "Microwave system to detect traumatic brain injuries using compact unidirectional antenna and wideband transceiver with verification on realistic head phantom," *IEEE Transactions on Microwave Theory and Techniques,* vol. 62, no. 9, pp. 1826-1836, 2014.

[58] I. Merunka, A. Massa, D. Vrba, O. Fiser, M. Salucci, and J. Vrba, "Microwave tomography system for methodical testing of human brain stroke detection approaches," *International Journal of Antennas and Propagation,* vol. 2019, 2019.

[59] F. Taher, A. Allam, A. F. Miligy, M. A. Mohamed, M. F. Abo Sree, and S. Y. A. Fatah, "Metamaterial Structure Effect on Printed Antenna for LTE/WIFI/Cancer Diagnosis," *Journal of Advanced Research in Applied Sciences and Engineering Technology,* vol. 46, no. 1, p. 237, 2025.

[60] M. S. B. Nesar, N. Chakma, M. A. Muktadir, and A. Biswas, "Design of a miniaturized slotted T-shaped microstrip patch antenna to detect and localize brain tumor," in *2018 International Conference on Innovations in Science, Engineering and Technology (ICISET)*, 2018, pp. 157-162: IEEE.

[61] A. Mobashsher and A. Abbosh, "Compact 3-D slot-loaded folded dipole antenna with unidirectional radiation and low impulse distortion for head imaging applications," *IEEE Transactions on Antennas and Propagation,* vol. 64, no. 7, pp. 3245-3250, 2016.

[62] A. T. Mobashsher, K. S. Bialkowski, and A. M. Abbosh, "Design of compact cross-fed three-dimensional slot-loaded antenna and its application in wideband head imaging system," *IEEE Antennas and Wireless Propagation Letters,* vol. 15, pp. 1856-1860, 2016.

[63] A. Salleh, C. C. Yang, M. S. J. Singh, and M. T. Islam, "Development of antipodal Vivaldi antenna for microwave brain stroke imaging system," *Int. J. Eng. Technol,* vol. 8, no. 3, pp. 162-168, 2019.

[64] B. Sohani *et al.*, "Detection of haemorrhagic stroke in simulation and realistic 3-D human head phantom using microwave imaging," *Biomedical Signal Processing and Control,* vol. 61, p. 102001, 2020.

[65] B. Han, S. Wang, and X. Shi, "Design of Compact Fragment-Type Antenna Array for Microwave-Based Head Imaging Application," *Journal of the Korean Institute of Electromagnetic and Science,* 2023.

[66] S. Y. Jun, B. S. Izquierdo, and E. A. Parker, "Liquid sensor/detector using an EBG structure," *IEEE Transactions on Antennas and Propagation,* vol. 67, no. 5, pp. 3366-3373, 2019.

[67] W. Zhang, J.-Y. Li, and J. Xie, "High sensitivity refractive index sensor based on metamaterial absorber," *Progress In Electromagnetics Research M,* vol. 71, pp. 107-115, 2018.

[68] R. Kumari, P. N. Patel, and R. Yadav, "An ENG resonator-based microwave sensor for the characterization of aqueous glucose," *Journal of Physics D: Applied Physics,* vol. 51, no. 7, p. 075601, 2018.

[69] A. M. Gargari, M. H. Zarifi, and L. Markley, "Passive matched mushroom structure for a high sensitivity low profile antenna-based material detection system," *IEEE Sensors Journal,* vol. 19, no. 15, pp. 6154-6162, 2019.

[70] M. T. Islam, M. R. Islam, M. T. Islam, A. Hoque, and M. Samsuzzaman, "Linear regression of sensitivity for meander line parasitic resonator based on ENG metamaterial in the application of sensing," *Journal of Materials Research and Technology,* vol. 10, pp. 1103-1121, 2021.

[71] N. Meyne, G. Fuge, A.-P. Zeng, and A. F. Jacob, "Resonant microwave sensors for picoliter liquid characterization and nondestructive detection of single biological cells," *IEEE journal of electromagnetics, RF and microwaves in medicine and biology,* vol. 1, no. 2, pp. 98-104, 2017.

[72] E. Massoni, G. Siciliano, M. Bozzi, and L. Perregrini, "Enhanced cavity sensor in SIW technology for material characterization," *IEEE Microwave and Wireless Components Letters,* vol. 28, no. 10, pp. 948-950, 2018.

[73] J. Wu *et al.*, "Design and validation of liquid permittivity sensor based on RCRR microstrip metamaterial," *Sensors and Actuators A: Physical,* vol. 280, pp. 222-227, 2018.

[74] M. Yadav, M. Ali, and R. Yadav, "A compact and economical AMC backed antenna solution for wearable biomedical applications," *International Journal of Microwave and Wireless Technologies,* vol. 15, no. 9, pp. 1514-1523, 2023.

[75] V. Jagadeesan *et al.*, "Design and development of a new metamaterial sensor-based Minkowski fractal antenna for medical imaging," *Applied Physics A,* vol. 129, no. 5, p. 391, 2023.

[76] S. Datta and L. Upda, "Microwave imaging sensor system using metamaterial lens for subwavelength resolution," *NDT & E International,* vol. 139, p. 102908, 2023.

[77] N. Wongkasem and G. Cabrera, "Multiple-Point Metamaterial-Inspired Microwave Sensors for Early-Stage Brain Tumor Diagnosis," *Sensors,* vol. 24, no. 18, p. 5953, 2024.

XXXX-XXXX © XXXX IEEE. Personal use is permitted, but republication/redistribution requires IEEE permission.
See http://www.ieee.org/publications_standards/publications/rights/index.html for more information.
This work is licensed under a Creative Commons Attribution 4.0 License. For more information, see https://creativecommons.org/licenses/by/4.0/

This article has been accepted for publication in IEEE Sensors Journal. This is the author's version which has not been fully edited and content may change prior to final publication. Citation information: DOI 10.1109/JSEN.2026.3668988

[78] N. M. Chowdhury *et al.*, "Interconnected four split rectangular ring resonator flexible metamaterial for microwave sensing application," *Scientific Reports,* vol. 15, no. 1, p. 21230, 2025.

[79] S. Shamim, A. S. Mohsin, M. M. Rahman, and M. B. H. Bhuian, "Recent advances in the metamaterial and metasurface-based biosensor in the gigahertz, terahertz, and optical frequency domains," *Heliyon,* vol. 10, no. 13, 2024.

MUSA N. HAMZA received the B.Sc. degree from the Department of Physics, Faculty of Science and Health, Koya University, Koysinjaq, Erbil, Iraqi Kurdistan, Iraq, in 2015, and the M.Sc. degree from the Department of Medical Physics, College of Medical and Applied Sciences, Charmo University, Chamchamal, Sulaymaniyah, in 2023. His research interests include medical physics, the diagnosis of different types of cancer at an early stage, antenna arrays, metamaterials, sensors, and biosensors.

MOHAMMAD TARIQUL ISLAM (Senior Member, IEEE) is currently a Professor with the Department of Electrical, Electronic and Systems Engineering, Universiti Kebangsaan Malaysia (UKM) and a Visiting Professor with the Kyushu Institute of Technology, Japan. He is the author and coauthor of about 800 research journal articles, nearly 250 conference articles, and a few book and book chapters on various topics related to antennas, metamaterials, and microwave imaging with 25 inventory patents filed. Thus far, his publications have been cited 20,700 times and his H-index is 63 (Source: Scopus). His Google scholar citation is 30,700 and H-index is 74. He was a recipient of more than 40 research grants from the Malaysian Ministry of Science, Technology and Innovation, Ministry of Education, UKM research grant, international research grants from Japan, Saudi Arabia and Kuwait. His research interests include communication antenna design, metamaterial, satellite antennas, and microwave imaging. Dr. Islam has been serving as an Executive Committee member for IEEE AP/MTT/EMC Malaysia Chapter, since 2019-2020, the Chartered Professional Engineer (CEng), a fellow of IET, U.K., and a Senior Member of IEICE, Japan. He received several International Gold Medal awards, a Best Invention in Telecommunication Award for his research and innovation, and best researcher awards at UKM. He was a recipient of 2018, 2019 and 2020 IEEE AP/MTT/EMC Malaysia Chapter, Excellent Award. He also won the best innovation award and the Best Researcher award by UKM, in different years. He was a recipient of Publication Award from Malaysian Space Agency, in several years. He has supervised about 70 Ph.D. theses, 30 M.Sc. theses, and has mentored more than 10 postdocs and Visiting scholars. He has developed the Antenna Measurement Laboratory which includes antenna design and measurement facility till 40 GHz. He was an Associate Editor of IET Electronics Letter. He also serves as the Guest Editor, SENSORS journal, Nanomaterials, and an Associate Editor for IEEE ACCESS and Editorial board Members for 'Scientific Reports' Journal by Springer Nature.

SLAWOMIR KOZIEL received the M.Sc. and Ph.D. degrees in electronic engineering from Gdansk University of Technology, Poland, in 1995 and 2000, respectively. He also received the M.Sc. degrees in theoretical physics and in mathematics, in 2000 and 2002, respectively, as well as the PhD in mathematics in 2003, from the University of Gdansk, Poland. He is currently a Professor with the Department of Engineering, Reykjavik University, Iceland. His research interests include CAD and modeling of microwave and antenna structures, simulation-driven design, surrogate-based optimization, space mapping, circuit theory, analog signal processing, evolutionary computation and numerical analysis.

Sunil Lavadiya working as Associate Professor in the Department of Information and Communication Technology at Marwadi University, Rajkot, Gujarat. He has completed his PhD on the topic of High Gain Frequency Reconfigurable Liquid Metamaterial Microstrip Patch Antenna. He has completed an M.Tech in communication engineering from Nirma University in 2010, and a B.Tech in Electronics and Communication from Saurashtra University in 2008. He has adapted to all aspects of Electronics and Communication Engineering, including training, education, and research. He works in the MIMO, Sensors, Reconfigurable, Superstrate, Solar absorber and liquid antennas. He is a member of professional bodies like IEEE and IETE. He has published 50 SCI research articles, 12 SCOPUS index articles, 8 book chapters, and 5 papers in an international conference and filed four design patents and one copyright.

Iftikhar ud din Received B.Sc. and M.Sc. Degree in Telecommunication Engineering from University of Engineering and Technology, Peshawar, Pakistan, in 2017 and 2021 respectively. He is the member of the Antennas & Microwave Engineering Research Group (AMERG) in UET Mardan. His current research interests include UWB antennas, FSS based UWB antennas and Sub-6 GHz 5G antennas, 5G millimeter wave antennas and MIMO antennas, frequency selective surfaces, EBGs and Metamaterial based antenna.

Bruno Cavalcante de Souza Sanches received the B.S. degree in information engineering and the M.Sc. degree in energy from the Federal University of ABC, Santo André, Brazil. He received the Ph.D. degree in microelectronics with the Integrated Systems Laboratory (LSI), University of São Paulo, São Paulo, Brazil, working in the design of a novel mixed signal integrated circuit used in the ALICE experiment in the CERN LHC. Bruno has more than fifteen years of experience in electronics and microelectronics design. He has been involved in hardware development, smart grids, algorithms, artificial intelligence, digital communication systems, EDA tools, electronics for high energy physics experiments and in several systems targeting early cancer detection including bioimpedance spectroscopy and microwave imaging.

Syeda Iffat Naqvi (Senior Member, IEEE) received her PhD Telecommunication Engineering degrees from University of Engineering and Technology, Taxila, Pakistan, in 2021. She is currently serving as Assistant Professor at University of Engineering and Technology, Taxila. She is working towards the design and implementation of MIMO antennas systems for millimeter-wave 5G and beyond wireless communication applications, metamaterials, Terahertz and Sub-Terahertz antennas, Beamsteerable antenna arrays, and Ridge Gap Waveguide based antennas. She has authored and co-authored numerous technical articles in ISI-indexed journals, and deliver a number of conference talks. She is also a frequent reviewer of various prestigious journals. Furthermore, she has served as Technical Committee member for a number of international conferences and as Guest Editor for various Special Journal Issues.

Abinash Panda (Senior Member, IEEE) received the B.Tech. and M.Tech. degrees in Electronics and Communication Engineering from Biju Patnaik University of Technology (BPUT), Odisha, India, and the Ph.D. degree from the National Institute of Technology Silchar, Assam, India. He subsequently worked as a Visiting Researcher at Slovak University of Technology Bratislava, Slovakia.and Postdoctoral Researcher at Chulalongkorn University, Bangkok, Thailand. He is currently working as Associate Professor in the department of Electronics and Communication Engineering at CMR Institute of Technology (CMRIT), Bengaluru, India. His research interests include photonic waveguides, photonic crystals, fiber and integrated photonics, bio-photonic and plasmonic sensors, optoelectronic devices, MEMS, and nanomaterial synthesis and characterization. His recent work focuses on 2D material-assisted SPR biosensors, advanced optical sensing platforms, and photonic device design for biomedical and environmental applications. He has published several research articles in reputed journals and conferences and is actively involved in IEEE activities, student mentoring, and interdisciplinary research collaborations.

Mohammad Naser-Moghadasi was born in Saveh, Iran, in 1959. He received the B.Sc. degree in Communication Eng. in 1985 from the Leeds Becket University (formerly Leeds polytechnic), UK. Between 1985 and 1987 he worked as an RF design engineer for the Gigatech company in Newcastle Upon Tyne, UK. From 1987 to 1989, he was awarded a full scholarship by the Leeds educational authority to pursue an M.Phil. Studying in CAD of Microwave circuits. He received his Ph.D. on design and construction of a hybrid dual mode cavity resonator filter in 1993, from the University of Bradford, UK. He was offered then a two years Post Doc. To pursue research on Microwave cooking of materials at the University of Nottingham, UK. From 1995 Dr. Naser-Moghadasi joined Islamic Azad University, Science & Research Branch, Iran, where he currently is full professor in Electrical Engineering. His main areas of interest in research are Microstrip antenna, Microwave passive and active circuits, RF MEMS and EMC. He has so far published over 250 peer reviewed papers in different journals and conferences.

Bal S. Virdee (SM'08) received the B.Sc. and MPhil degrees in Communications Engineering from the University of Leeds, UK, and his Ph.D. in Electronic Engineering from the University of London, UK. He has worked in industry for various companies including Philips (UK) as an R&D-engineer and Teledyne Defence and Space as a future products developer in RF/microwave communications. He has taught at several academic institutions before joining London Metropolitan University where he is a Senior Professor of Communications Technology in the School of Computing and Digital Media where he is Head the Communications Technology Research Center. His research, in collaboration with industry and academia, is in wireless communications encompassing mobile-phones to satellite-technology. Prof. Virdee has chaired technical sessions at IEEE international conferences and published numerous research papers. He is Executive Member of IET's Technical and Professional Network Committee on RF/Microwave-Technology. He is a Fellow of IET and a Senior-Member of IEEE.

Ali Farmani (Member, IEEE) received the B.Sc. degree in electrical engineering from the Shiraz University of Technology in 2008, the M.Sc. degree in electrical engineering from the University of Tabriz in 2010, and the Ph.D. degree in electrical engineering from Shiraz University in 2017. During his stay at Lorestan University as an Assistant Professor (2018–2024), he has mentored several B.Sc., ten M.Sc. theses, and four Ph.D. dissertations. He is the author of more than 106 ISI papers and three book chapters. His research interests are VLSI, nanoelectronics, plasmonics, and investigation of new materials for integrated photonics. He was a recipient of the fellowship for Ph.D. study at Shiraz University as an

XXXX-XXXX © XXXX IEEE. Personal use is permitted, but republication/redistribution requires IEEE permission.
See http://www.ieee.org/publications_standards/publications/rights/index.html for more information.
This work is licensed under a Creative Commons Attribution 4.0 License. For more information, see https://creativecommons.org/licenses/by/4.0/

This article has been accepted for publication in IEEE Sensors Journal. This is the author's version which has not been fully edited and content may change prior to final publication. Citation information: DOI 10.1109/JSEN.2026.3668988

Exceptional Talent. He received the Shiraz Distinguished Ph.D. Dissertation Award for his work on plasmonic nanostructures. He was also a recipient of the Excellent Reviewer Award from Elsevier and IEEE Journals (2017–2024).

Patrizia Livreri, IEEE Senior member, received the Laurea degree (Hons.) in electronics engineering, and the Ph.D. degree in electronics and communications engineering from the University of Palermo, Italy, in 1986 and 1992, respectively. From 1993 to 1994, she was a Researcher with the National Council for Researches, CNR, Rome, Italy. Since 1995, she has been the Scientific Director for the Microwave Instruments and Measurements Laboratory with the Department of Engineering, University of Palermo. In 2020, she also joined the CNIT National Laboratory for Radar and Surveillance Systems RaSS, Pisa. She is currently a professor at the Department of Engineering, University of Palermo, and a visiting professor at San Diego State University. She is a Principal Investigator of the "Microwave Quantum Radar" project, funded by the Ministry of Defense, in 2021. Her research interests include microwave and millimeter vacuum high power (TWT, Klystron) and solid-state power amplifiers for radar applications; high power microwave sources (virtual cathode oscillator and magnetically insulated transmission line oscillator); microwave and optical antennas; radar; and microwave quantum radar. Prof. Livreri is the author or co-author of more than 250 publications in prestigious International Journals and Conferences. In 2024, she has been nominated IEEE Aerospace and Electronic Systems Distinguished Lecturer.

MD. SHABIUL ISLAM (Senior Member, IEEE) received the B.Sc. (Hons.) and M.Sc. degrees from the Department of Applied Physics and Electronics, Rajshahi University, Bangladesh, in 1986 and 1985, respectively, the M.Sc. degree (by research) in micro controller based system design from the Department of Electrical, Electronics and System Engineering, Universiti Kebangsaan Malaysia (UKM), Bangi, Malaysia in 1997, and the Ph.D. degree in VLSI design from the Faculty of Engineering (FOE), Multimedia University (MMU), Cyberjaya, Malaysia, in 2008. From 1991 to 1993, he was a Scientific Officer with The Institute of Electronics and Material Science (IEMS), Bangladesh Atomic Energy Commission (BAEC), Saver, Dhaka, Bangladesh. From July 1999 to July 2009, he was a Lecturer with the Faculty of Engineering, MMU. From July 2009 to March 2012, he was a Senior Lecturer with IMEN, UKM. From June 2010 to December 2012, he was an Associate Fellow with the Department of Electrical, Electronics and System Engineering, Faculty of Engineering and Built Environment, UKM. From March 2012 to December 2016, he worked as an Associate Professor with The Institute of Microengineering and Nanoelectronics (IMEN), UKM. From April 2017 to March 2020, he was an Associate Fellow with IMEN, UKM. He is currently a Professor with the Faculty of Engineering, Multimedia University. He is also the Head of the Micro/Nano Electronics System (MiNES) Laboratory, IMEN. His expertise covers a wide range of engineering disciplines, including micro/nano system design, VLSI design, microcontroller based system design, micro-powering harvesting, and digital communication system. He received internal & external research funds for doing his research work at IMEN, UKM, from 2010 to 2016. His research support also partly contributed to the award of the Higher Education Center of Excellence (HiCOE) from the Malaysian government to IMEN recently. He has published 78 ISI & SCOPUS, five research books, one chapter in book, and 90 conference proceeding. He filed one patent. He is a member of the IEEE Circuits and Systems Society, a Member of the Bangladesh Electronics Society, and an Associate Member of Bangladesh Computer Society (AM476).

Nisar Ahmad Abbasi received his B.Sc. degree (with honors) in electrical and electronic engineering from the University of Engineering and Technology, Peshawar, Pakistan, in 2001, and his M.Sc. and Ph.D. degrees in electronic engineering from the University of Sheffield, Sheffield, UK, in 2007 and 2011, respectively. He has held various positions, such as assistant manager, manager, and general manager, while working for the Ministry of Science, Pakistan, between 2001 and 2016. He was an assistant professor at the University of Hafr Al Batin, Hafr Al Batin, KSA between 2017 and 2025. He is currently an associate professor at Bahrain Polytechnic, Bahrain. His research interests include the design and analysis of various antenna types and telecommunication networks. Dr. Abbasi is a professional engineer (PE) in Pakistan and a member of the Pakistan Engineering Council (PEC).

Mohammad Alibakhshikenari (Member, IEEE) was born in Mazandaran, Iran, in February 1988. He received the Ph.D. degree with the European label and Excellent Cum Laude in electronics engineering from the University of Rome ''Tor Vergata'' (UNITOV), Italy, in February 2020. From May 2018 to December 2018, he was a Ph.D. Visiting Researcher with the Chalmers University of Technology, Gothenburg, Sweden. His training during this visit included a research stage at Swedish Company "Gap Waves AB." During his Ph.D. (Nov. 2016 – Feb. 2020), he was recognized as the winner of 13 grants for attending the Doctoral Schools organized by ESoA (European School of Antennas, 5), EUPROMETA (European Doctoral Programmes in Metamaterials, 3), EuMC (European Microwave Conference, 2), SIE (Società Italiana di Elettronica - Italian Society of Electronics, 1), ITMO University (Nanophotonics and Metamaterials, 1), Aix-Marseille Université (Metamaterials, 1), which were held in various European universities. He successfully achieved all 30 credits provided by Doctoral Schools leading him to obtain his Ph.D. degree with European label. He is now a Marie Sklodowska-Curie, ROSETTA, and LERO (the Research Ireland Centre for Software) Fellow at the University of Galway, Ireland. As part of this fellowship, he had five research visits at the Microwave Engineering Center for Space Applications (MECSA, October 2025); Universitat Ramon Llull, Barcelona, Spain (October 2025); Institute of Science Tokyo, Japan (November 2025); Pusan National University, Busan, South Korea (December 2025); and Sogang University, Seoul, South Korea (December 2025). From September 2024 to June 2025, he was with UNITOV as a Senior Researcher. From July 2021 to August 2024, he was with the Department of Signal Theory and Communications, Universidad Carlos III de Madrid (uc3m), Spain, as a Marie Sklodowska-Curie and CONEX-Plus Fellow. During this Program he has spent two secondments at the: 1) Microwave Engineering Center for Space Applications (MECSA), Rome, Italy, from April to August 2024, and 2) SARAS Technology Ltd., Company, Leeds, U.K., from December 2022 to May 2023. In addition, during this program he had one-week research visits at the: 1) University of Catania, Italy, in May 2024, along with an invited lecture entitled ''Terahertz Antennas based on Metasurface and SIW'' for the master's and Ph.D. students, and postdoctoral researchers; 2) University of Messina, Italy, in May 2024; 3) University of Bradford, U.K., in May 2023; and 4) Edinburgh Napier University, U.K., in April 2023. For academic year 2021 and 2022, he received the "Teaching Excellent Acknowledgement" certificate for the course of "electromagnetic fields" from the Vice-Rector of studies of UC3M. In November 2019, he was winner of a postdoctoral research fund for two years awarded by UNITOV. His research interests include "Electromagnetic fields, antennas and wave-propagations, metamaterials and metasurfaces, RF and microwave technologies, sensors, wireless communications, multiple input multiple output (MIMO) systems, millimeter-waves and terahertz integrated circuits, gap waveguide technology, and beamforming networks". His research activities are documented in about 200 papers published in international journals, 1 book, 9 book chapters, and about 112 papers in proceedings of international conferences including 49 in-person presentations in 31 conferences and 27 on-line presentations in 13 conferences (the rest were presented by my colleaguses). His research works received more than 9000 citations with H-index above 58 reported by Scopus, Google Scholar, and ResearchGate. According to Stanford University yearly analysis, he has been among the World's Top 2% Scientists of highly cited scientific authors, since 2020. He was listed in both Career Long and Single Year Impact in Stanford's list. He was a recipient of two young engineer awards of the 47th and 48th European Microwave Conferences held in Nuremberg, Germany, in 2017, and in Madrid, Spain, in 2018, respectively. In April 2020, his research article entitled ''High-Gain Metasurface in Polyimide On-Chip Antenna Based on CRLH-TL for Sub Terahertz Integrated Circuits, published in Scientific Reports, volume 10, Article number 4298 (2020)'' was awarded as the Best Month Paper at the University of Bradford, U.K. In addition, he serves the role of an Associate Editor for two scientific journals of Radio Science and The Journal of Engineering (IET). He acts as a referee in several journals, and the technical program committee (TPC) and session chair of several international conferences. In addition, he is member of the reviewer panel of Dutch Research Council (NWO); U.K. Research and Innovation (UKRI) Funding Service; IEEE MTT-S Education Committee Fellowships and Scholarships; and the External Examiner of several Ph.D. dissertations from various worldwide universities.

XXXX-XXXX © XXXX IEEE. Personal use is permitted, but republication/redistribution requires IEEE permission.
See http://www.ieee.org/publications_standards/publications/rights/index.html for more information.
This work is licensed under a Creative Commons Attribution 4.0 License. For more information, see https://creativecommons.org/licenses/by/4.0/